RESEARCH ARTICLE





Computational multiphase periporomechanics for unguided cracking in unsaturated porous media

Shashank Menon | Xiaoyu Songo

Engineering School of Sustainable Infrastructure & Environment, University of Florida, Gainesville, Florida, USA

Correspondence

Xiaoyu Song, Engineering School of Sustainable Infrastructure & Environment, University of Florida, Gainesville, FL 32611, USA. Email: xysong@ufl.edu

Funding information

National Science Foundation, Grant/Award Numbers: 1659932, 1944009

Abstract

In this article, we formulate and implement a computational multiphase periporomechanics paradigm for unguided fracturing in unsaturated porous media assuming passive pore air pressure. The same governing equation for the solid phase applies on and off cracks. Crack formation in this framework is autonomous, requiring no prior estimates of crack topology. As a new contribution, an energy-based criterion for arbitrary crack formation is formulated using the peridynamic effective force state for unsaturated porous media. Unsaturated fluid flow in the fracture space is modeled in a simplified way in line with the nonlocal formulation of unsaturated fluid flow in the bulk. The formulated unsaturated fracturing periporomechanics is numerically implemented through an implicit fractional step algorithm in time and a two-phase mixed meshless method in space. The two-stage operator split converts the coupled periporomechanics problem into an undrained deformation and fracture problem and an unsaturated fluid flow in the deformed skeleton configuration. Numerical simulations of in-plane open and shear cracking are conducted to validate the accuracy and robustness of the fracturing unsaturated periporomechanics model. Then numerical examples of wing cracking and nonplanar cracking in unsaturated soil specimens are presented to demonstrate the efficacy of the proposed multiphase periporomechanics paradigm for unguided cracking in unsaturated porous media.

KEYWORDS

fracture fluid flow, nonlocal, periporomechanics, unguided cracking, unsaturated porous media

1 | INTRODUCTION

The mechanical and physical behavior of unsaturated porous media (e.g., unsaturated soils) plays a significant role in resilience and sustainability of civil infrastructures (e.g., References 1-11). Cracking in unsaturated soils can significantly deteriorate and compromise the integrity of civil infrastructures built on such materials (e.g., References 12-15). For instance, the volume shrinkage by variations of matric suction (i.e., the difference between pore air and water pressures) could generate tensile cracks in unsaturated soils. The bearing capacity of structural foundations on such soils can be significantly reduced by the presence of tensile cracks. Surface cracks caused by the rapid drawdown of a reservoir can be a trigger for landslides. Desiccation cracking in clay can dramatically increase its hydraulic conductivity that will compromise its ability to act as liner material for landfills. With the advance of supercomputers, computational methods

play an increasingly significant role in modeling the mechanical and physical behavior including cracking of unsaturated soils (e.g., Reference 9). In this study, different from the celebrated computational methods such as the extended finite element method (e.g., References 17 and 18) and as a new contribution, we develop a fully coupled nonlocal mathematical paradigm for modeling fracturing and fluid flow in unsaturated porous media using periporomechanics (e.g., References 19-24 and see Section 2.1 for a brief review) that is a nonlocal reformulation of classical poromechanics ²⁵⁻²⁷ through peridynamics^{28,29} for modeling variably saturated porous media. We refer to the celebrated literature (see References 13 and 14, among many others) on other robust computational techniques for modeling cracking in fracturing porous media under variably saturated conditions. Note that the original peridynamics was proposed by Silling for modeling deformation and cracks in single-phase solid materials. In the proposed periporomechanics model the same momentum balance equation applies on and off the crack surface by using the effective force state concept, ²² as in the classical peridynamics for modeling cracks in solids. Next, we briefly review the application of peridynamics for modeling cracks focusing on the criterion of initiation and propagation of cracks.

In peridynamics, cracks nucleate, grow, branch, and merge when and where it is energetically favorable for them to do so according to the global equations and constitutive model (e.g., References 30 and 31). This salient feature of autonomous crack growth obviates the need for the remedial techniques of classical fracture mechanics. We refer to the literature (e.g., Reference 32) for an in-depth comparison of peridynamics and classical fracture mechanics.³³ Peridynamics has been applied to model fractures in solids (e.g., References 34-40, among many others) and porous media (e.g., References 15 and 41-45, among others). There are two criteria for the inception and propagation of cracks, namely "bond-breakage" using either a kinematic criterion (stretch, shear) (e.g., References 15, 34, and 46-49) and a strain energy criterion (e.g., References 43 and 50-53). In the kinematic-based criterion, peridynamic bonds are assumed to fail irreversibly when the relative extension exceeds a predetermined limit value called "critical stretch." This criterion has some limitations including its ad-hoc feature, its inability to correctly model shear cracks, and its apparent lack of any rational basis or theoretical justification for the link between critical stretch and crack energy release rate. In the energy based criterion, the elastic strain energy is correlated to the fracture potential energy. Madenci and Oterkus⁵² proposed an energy-based failure criterion for fracture, based on the peridynamic equivalent of the classical J-integral.⁵⁴ Breitenfeld et al.⁵¹ formulated a peridynamic equivalent of the *J*-integral to extract the classical stress intensity factors of linear elastic fracture mechanics as a means of examining the stress singularities. Lipton et al.⁵³ developed an elastic peridynamic material based on a novel strain energy density function capable of modeling cracks. In this method, cracks are modeled as material instability in the softening regime allowing spontaneous nucleation of cracks without the assistance of supplemental criteria. Note that both criteria have been utilized to model fracture in porous media (e.g., References 15, 44, and 55) through the effective stress concept for porous media. 1,25 In this article, as a new contribution, in the fracturing unsaturated periporomechanics paradigm we develop an energy-based crack criterion through the recently proposed effective force state concept²² for unsaturated porous media.

In Reference 24, the authors formulated a stabilized coupled periporomechanics model for dynamic analysis of saturated porous media with no cracks. In the present article, as a new contribution the formulation in Reference 24 is extended to model unguided fracturing and fluid flow in unsaturated porous media. In this fracturing unsaturated periporomechanics model, the same governing equation for the solid phase applies on and off cracks. In line with the original peridynamics, ^{28,29,56} crack formation in this coupled framework is autonomous, requiring no prior estimates of crack topology. As a major novelty, the criterion for arbitrary and unguided crack formation in three dimensions (e.g., nonplanar) is formulated based on the peridynamic effective force state for unsaturated porous media. Unsaturated fluid flow in the fracture space is coupled to the fluid flow in the bulk through a leak-off term. Different from the fully coupled numerical implementation in Reference 24, the formulated unsaturated fracturing periporomechanics is numerically implemented through the celebrated fractional step algorithm (also called staggered algorithm in the literature, see Reference 13, 25, 26, 44, 55, and 57-59, and others) for computational efficiency and accuracy. The two-stage operator split converts the coupled fracturing periporomechanics problem into an undrained deformation and fracture problem and an unsaturated fluid flow problem in the deformed configuration. Note that we refer to the literature for explicit or implicit implementation of peridynamics for modeling cracks in single-phase solids (e.g., References 51, 56, and 60-63, among others). Numerical simulations are conducted to validate the accuracy and robustness of the computational fracturing unsaturated periporomechanics paradigm. We run numerical simulations of crack propagation in porous media and analyze the influence of initial matric suction and intrinsic permeability on the wing crack propagation. Finally, we demonstrate the efficacy of the proposed fracturing periporomechanics paradigm for modeling nonplanar cracks by simulating nonplanar cracks triggered by varying matric suction in a three-dimensional soil specimen.

The original contributions of this article are (i) the formulation of the energy-based crack criterion based on the effective force state concept for unsaturated porous media, (ii) the implicit fractional-step and mixed meshless numerical implementation of the fracturing unsaturated periporomechanics paradigm in time and space, and (iii) the validation of the numerical implementation by comparing numerical results from this newly formulated method with the classical extended finite element method and demonstration of the new coupled framework for modeling nonplanar cracks in unsaturated soils. For sign convention, the assumption in continuum mechanics is followed, that is, for solid skeleton tension is positive and compression is negative, and for pore fluid compression is positive and tension is negative.

2 | UNSATURATED FRACTURE PERIPOROMECHANICS FOR UNGUIDED CRACKING

2.1 Unsaturated periporomechanics

Periporomechanics is a reformulation of classical poromechanics through the peridynamic state concept²⁹ for modeling continuous or discontinuous deformation and fluid flow in variably saturated porous media. ^{19,21-24} In periporomechanics, it is hypothesized that a porous material body can be represented by a finite number of mixed material points that are endowed with two kinds of degree of freedom, that is, solid displacement and fluid pressure. It is a fully coupled strong nonlocal theory in that a material point x has direct poromechanical and physical interactions with any material point x' in its nonlocal family \mathcal{H} , ²⁹ a spherical domain centered at x. The radius of \mathcal{H} denoted by δ is called the *horizon* of the porous media. For conciseness of notations, it is assumed that a peridynamic state variable without a prime is evaluated at x on the associated bond $\xi = x' - x$ and the peridynamic state variable with a prime is evaluated at x' on the associated bond $\xi' = x - x'$, for example, $\underline{T} = \underline{T}[x]\langle x' - x \rangle$ and $\underline{T}' = \underline{T}[x']\langle x - x' \rangle$. Similarly, a non-state variable without a prime is associated with x and that with a prime is associated with x', for example, S_r is the degree of saturation at x'.

In unsaturated periporomechanics, 22 under the assumption of passive air pressure the balance of linear momentum at \boldsymbol{x} reads

$$\int_{\mathcal{H}} \left[\left(\underline{\overline{T}} - S_r \underline{T}_w \right) - \left(\underline{\overline{T}}' - S_r' \underline{T}_w' \right) \right] dV' + \rho \mathbf{g} = \rho \ddot{\mathbf{u}}, \tag{1}$$

where $\overline{\underline{T}}$ and $\overline{\underline{T}}'$ are the effective force states at x and x', respectively, $\underline{\underline{T}}_w$ and $\underline{\underline{T}}'_w$ are the pressure force states at x and x' respectively, S_r is the degree of saturation at x, g is the gravity acceleration, \ddot{u} is the acceleration, and ρ is the density of unsaturated porous media

$$\rho = \rho_{\rm S}(1 - \phi) + S_r \phi \rho_{\rm W},\tag{2}$$

where ρ_s is solid density, ρ_w is water density and ϕ is porosity. Under the assumptions of incompressible solid grain and water the balance of mass at x reads

$$\phi \frac{\mathrm{d}S_r}{\mathrm{d}t} + S_r \int_{\mathcal{H}} (\dot{\underline{\mathcal{V}}}_s - \dot{\underline{\mathcal{V}}}_s') \, \mathrm{d}V' + \frac{1}{\rho_w} \int_{\mathcal{H}} \left(\underline{Q} - \underline{Q}' \right) \, \mathrm{d}V' + \mathcal{Q}_s = 0, \tag{3}$$

where $\underline{\dot{\mathcal{V}}}_s$ and $\underline{\dot{\mathcal{V}}}_s'$ are the solid volume change rate states at \boldsymbol{x} and $\boldsymbol{x'}$, respectively, \underline{Q} and $\underline{Q'}$ are the fluid flow states at \boldsymbol{x} and $\boldsymbol{x'}$, respectively, and Q_s is a source/sink term.

The deformation state and pore fluid pressure state are essential state variables to construct constitutive models in periporomechanics. The deformation state \underline{Y} at x reads

$$Y = y' - y, \tag{4}$$

where y' and y are the deformed positions of x' and x, respectively. Let u and u' be displacements at x and x', respectively,

$$y = x + u, \quad y' = x' + u'.$$
 (5)

The fluid flow/pressure potential state at x reads

$$\Phi = p_w' - p_w,\tag{6}$$

where p_w and p'_w are water pressures at x and x', respectively.

In line with the stabilized multiphase correspondence principle,²⁴ the effective force state and unsaturated fluid flow state can be written as follows. First, the effective force state with stabilization reads

$$\underline{\overline{T}} = \underline{\omega} \left(\overline{P} K^{-1} \xi + \frac{GC}{\omega_0} \underline{\mathcal{R}}^s \right), \quad C = \frac{18K}{\pi \delta^4}, \tag{7}$$

where $\underline{\omega}$ is the influence function (also called weighting function), \overline{P} is the effective Piola–Kirchhoff stress tensor, K is the shape tensor, \underline{S}^s is the residual deformation state (see Equation 10), G is a positive constant on the order of 1, and K is the elastic bulk modulus of the skeleton, and ω_0 is defined as

$$\omega_0 = \int_{\mathcal{H}} \underline{\omega} \, dV'. \tag{8}$$

The shape tensor K is defined as

$$\mathbf{K} = \int_{\mathcal{H}} \underline{\omega} \boldsymbol{\xi} \otimes \boldsymbol{\xi} \, dV'. \tag{9}$$

The residual deformation state $\underline{\mathscr{R}}^s$ is defined as

$$\mathcal{R}^{s} = \underline{Y} - \widetilde{F}\xi. \tag{10}$$

It is noted that for a uniform deformation the residual deformation state \mathcal{R}^s is null.

The effective Piola-Kirchhoff stress tensor^{64,65} is defined as

$$\overline{P} = P + J(S_r p_w \mathbf{1}) \widetilde{F}^{-T}, \tag{11}$$

where P is the total Piola–Kirchhoff stress tensor, $\mathbf{1}$ is the second-order identity tensor, and J is the determinant of \tilde{F} that is the nonlocal deformation gradient

$$\widetilde{F} = \left(\int_{\mathcal{H}} \underline{\omega} \ \underline{Y} \otimes \xi \ dV' \right) K^{-1}. \tag{12}$$

Given \tilde{F} the effective Piola–Kirchhoff stress tensor \overline{P} can be determined through the classical constitutive models for unsaturated soils. Let ϕ_0 be the initial porosity, the porosity in (3) can be written as⁶⁴

$$\phi = 1 - (1 - \phi_0)/J. \tag{13}$$

Similarly, the fluid flow state with stabilization at x^{22} is written as

$$\underline{Q} = \underline{\omega} \left(\rho_w \mathbf{q} \mathbf{K}^{-1} \boldsymbol{\xi} + \frac{G K_p}{\omega_0} \underline{\mathscr{R}}^w \right), \quad K_p = \frac{6 \rho_w k_w}{\pi \delta^4 \mu_w}, \tag{14}$$

where \mathbf{q} is the fluid flux vector, $\underline{\mathcal{R}}^{w}$ is the residual pressure potential state, k_{w} is the intrinsic permeability, and μ_{w} is water viscosity. The fluid flux \mathbf{q} can be determined by the generalized Darcy's law for unsaturated fluid flow as

$$\mathbf{q} = -\frac{k^r k_w}{\mu_w} \widetilde{\mathbf{V}} \widetilde{\mathbf{\Phi}}, \quad \widetilde{\mathbf{V}} \widetilde{\mathbf{\Phi}} = \left(\int_{\mathcal{H}} \underline{\omega} \, \underline{\mathbf{\Phi}} \, \boldsymbol{\xi} \, \mathrm{d}V' \right) \mathbf{K}^{-1}, \tag{15}$$

where k^r is the relative permeability and $\widetilde{\nabla \Phi}$ is the nonlocal fluid pressure gradient. The residual fluid potential state $\underline{\mathscr{R}}^w$ is defined as

$$\underline{\mathscr{R}}^{w} = \underline{\Phi} - \widetilde{\nabla} \Phi \xi. \tag{16}$$

Note that $\underline{\mathscr{R}}^w$ is null for a uniform fluid pressure potential. Here, the soil–water retention curve 66-68 is described by the celebrated van Genuchen equation 69 as

$$S_r = S_1 + (S_2 - S_1) \left[1 + \left(\frac{s}{s_a} \right)^n \right]^{(1-n)/n}, \tag{17}$$

where *s* is matric suction (e.g., $s = -p_w$ assuming passive air pressure), and S_1 , S_2 , S_a , and *n* are material constants. In this study, it is assumed that $S_1 = 0$ and $S_2 = 1$. Given S_r the relative permeability k_r can be written as

$$k^{r} = S_{r}^{1/2} \left[1 - (1 - S_{r}^{1/m})^{m} \right]^{2}, \tag{18}$$

where m = (n-1)/n.

Next, we present a formulation of so-called ordinary material models for unsaturated porous media that do not exhibit the same instability observed in the original correspondence material models. Here the ordinary means that the force state is parallel to the bond ξ . Let $y = |\underline{Y}|$, the total force state reads

$$\underline{T} = \left(\underline{\bar{t}} - S_r \underline{t}_w\right) \left(\underline{\frac{Y}{Y}}\right),\tag{19}$$

where \bar{t} and \underline{t}_w are the scalar effective force state and the scalar water pressure state, respectively. For a poroelastic material, the scalar effective force state \bar{t} can be defined as

$$\underline{\bar{t}} = \underline{\omega} \left(\frac{3K}{m_{\nu}} \theta \underline{x} + \frac{15\mu_{s}}{m_{\nu}} \underline{e}^{d} \right), \tag{20}$$

where $\underline{x} = |\xi|$, θ is the dilatation, $\underline{e}^d = \underline{e} - (\theta \underline{x}/3)$ is a measure of deviatoric deformation, $\underline{e} = \underline{y} - \underline{x}$, m_v is the weighted volume, and K is the elastic bulk modulus as introduced previously, and μ_s the elastic shear mudulus of the skeleton.

$$m_{\nu} = \int_{\mathcal{H}} \underline{\omega} \, \underline{x}^2 \, \mathrm{d}V', \tag{21}$$

$$\theta = \frac{3}{m_v} \int_{\mathcal{H}} \underline{e} \, \underline{x} \, \mathrm{d}V'. \tag{22}$$

In line with Equation (20), the water pressure scalar state in (19) can be defined as

$$\underline{t}_{w} = \underline{\omega} \frac{3p_{w}\underline{x}}{m_{w}},\tag{23}$$

From (19) and (20), the effective force state through the ordinary material model for the solid skeleton reads

$$\overline{\underline{T}} = \overline{\underline{t}} \left(\frac{\underline{\underline{Y}}}{\underline{\underline{y}}} \right). \tag{24}$$

We note that the ordinary material model in (24) is a special case of the general correspondence material model in (7). To support this statement, we first demonstrate that the shape tensor can be expressed by the weighted volume in what follows. The spherical coordinate system in Figure 1 is adopted to facilitate the derivation. Given the notations in Figure 1, the components of ξ in the Cartesian coordinate system read

$$\xi_1 = x \sin \overline{\alpha}_1 \sin \overline{\alpha}_2,\tag{25}$$

$$\xi_2 = x \cos \overline{\alpha}_1,\tag{26}$$

$$\xi_3 = \underline{x} \sin \overline{\alpha}_1 \cos \overline{\alpha}_2. \tag{27}$$

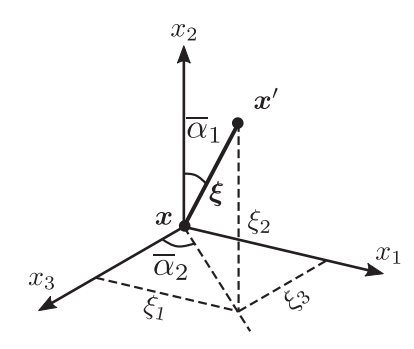


FIGURE 1 Two material points in the spherical coordinate system

Let $\omega = 1$ the weighted volume m_{ν} is written as

$$m_{\nu} = \int_{0}^{\delta} \int_{0}^{2\pi} \int_{0}^{\pi} \underline{x}^{4} \sin \overline{\alpha}_{1} d\overline{\alpha}_{2} d\underline{x}$$
$$= \frac{4\pi\delta^{5}}{5}. \tag{28}$$

Similarly, the shape tensor can be written as

$$K_{ij} = \int_{\mathcal{H}} \underline{\omega} \xi_{i} \xi_{j} dV'$$

$$= \int_{0}^{\delta} \int_{0}^{2\pi} \int_{0}^{\pi} \underline{\omega} \, \xi_{i} \xi_{j} \underline{x}^{2} \sin \overline{\alpha}_{1} \, d\overline{\alpha}_{2} \, d\underline{x}, \qquad (29)$$

where i, j = 1, 2, 3. It follows from (25), (26), (27), and (29) that for $\omega = 1$ we can readily show

$$K_{ij} = \frac{4\pi\delta^5}{15}\delta_{ij}. (30)$$

From (28) and (30), the shape tensor can be written as

$$\mathbf{K} = (m_v/3)\mathbf{1}.\tag{31}$$

Given (31), we can establish the equivalence between correspondence material models and ordinary material models for unsaturated porous media in what follows. Let us assume an isotropic deformation of unsaturated porous media

$$\mathbf{Y} = (1 + \varepsilon)\boldsymbol{\xi},\tag{32}$$

where ε is a constant scalar and $|\varepsilon| \ll 1$. Then from (12) and (30), the nonlocal deformation gradient can be written as

$$\widetilde{F} = (1 + \varepsilon)\mathbf{1}.\tag{33}$$

It follows from (7), (11) and the assumption $|\varepsilon| \ll 1$ that the total force state can be written as

$$\underline{T} = \underline{\omega} \left(\overline{\sigma} + S_r p_w \mathbf{1} \right) (\mathbf{1}) \left(\frac{3}{m_v} \mathbf{1} \right) \xi$$

$$= \underline{\omega} \left(3K \varepsilon \mathbf{1} + S_r p_w \mathbf{1} \right) \left(\frac{3}{m_v} \mathbf{1} \right) \underline{x} \frac{(1+\varepsilon) \xi}{(1+\varepsilon) \underline{x}}$$

$$= \underline{\omega} \left(K\theta + S_r p_w \right) \frac{3\underline{x}}{m_v} \frac{\underline{Y}}{\underline{y}}.$$
(34)

By (34), we demonstrate that under small isotropic deformation the total force state obtained from the correspondence material model is equivalent to the one obtained from the ordinary material model. With (31), the nonlocal pressure gradient and water flow state can also be written as follows.

$$\widetilde{\nabla \Phi} = \frac{3}{m_v} \left(\int_{\mathcal{H}} \underline{\omega} \, \underline{\Phi} \boldsymbol{\xi} \, dV' \right) \mathbf{1} = \frac{3}{m_v} \int_{\mathcal{H}} \underline{\omega} \, \underline{\Phi} \boldsymbol{\xi} \, dV', \tag{35}$$

$$\underline{Q} = \frac{3}{m_{\nu}}\underline{\omega}\rho_{\nu}\mathbf{q}(\mathbf{1}\boldsymbol{\xi}) = \frac{3}{m_{\nu}}\underline{\omega}\rho_{\nu}\mathbf{q}\boldsymbol{\xi}.$$
(36)

2.2 | Fracture unsaturated periporomechanics

In this section, we present fracture unsaturated periporomechanics that extends unsaturated periporomechanics to model fracture in unsaturated porous media. In fracture periporomechanics, both bulk and fracture space are represented by mixed material points that have two types of degree of freedom, that is, displacement and fluid pressure. The fracturing process in periporomechanics is modeled following the bond-breakage concept in the original peridynamics for solids. Figure 2 schematically represents the bond-breakage concept for modeling fracture formation in unsaturated periporomechanics. The broken poromechanical bond will not be considered when determining the effective force state at material point x through the constitutive model. The effective force state is zero on the broken poromechanical bond while pore fluid pressure remains. To facilitate the modeling of unsaturated fluid flow in fracture space, the mixed material point in fracture space is named fracture point that has two fluid pressures, that is, bulk fluid pressure p_w and fracture fluid pressure p_f .

2.2.1 | Fracture criterion based on the effective force state concept

The bond breakage can be modeled either by the critical stretch criterion or energy criterion (e.g., References 28 and 50). In unsaturated porous media, the bond-breakage can be triggered by deformation or matric suction in unsaturated porous media as illustrated by the energy-based criterion in what follows. In this study, the bond-breakage criteria in unsaturated periporomechanics are based on the deformation energy stored in a poromechanical bond. The effective force state that is an energy conjugate of the deformation state²² is used to determine the deformation energy, which is different from the single-phase peridynamics analysis. The effective force principle captures the effect of pressure developed in the pore fluid on the mechanical response of the skeleton. It is assumed that the energy density stored in a solid bond, $\underline{\omega}\langle\xi\rangle$, is fully recoverable until it exceeds some critical value ω_{cr} . With effective force state the energy density in a solid bond ξ reads

$$\underline{\underline{w}} = \int_{0}^{t_{l}} \left(\underline{\underline{T}} - \underline{\underline{T}}' \right) \dot{\boldsymbol{\eta}} \, dt = \int_{0}^{t_{l}} \left[\left(\underline{\underline{T}} + S_{r} \underline{\underline{T}}_{w} \right) - \left(\underline{\underline{T}}' + S'_{r} \underline{\underline{T}}'_{w} \right) \right] \dot{\boldsymbol{\eta}} \, dt, \tag{37}$$

where $\eta = u' - u$ is the relative displacement vector and t_l is the total loading time. It is noted that the energy-based criterion of (37) incorporates the coupling effect of skeleton deformation, matric suction, and degree of saturation on the

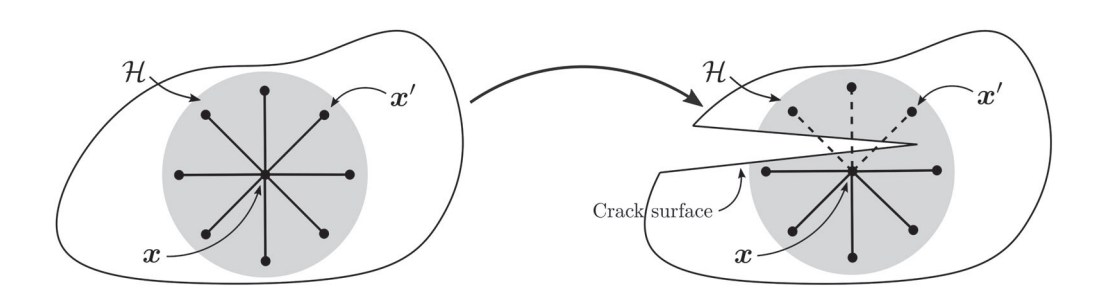


FIGURE 2 Conceptual sketch of fracturing in periporomechanics: (A) A material point in a porous body and (B) a material point with bond breakage in a fractured porous body

bond breakage. In fracture unsaturated periporomechanics, bond breakage is modeled through the influence function at the material constitutive model level for the solid and fluid phases. The influence function will be replaced by a new influence function $\rho\omega$, where ρ is defined as

$$\underline{\varrho} = \begin{cases} 0, & \text{if } \underline{\varpi} \ge \varpi_{cr}, \\ 1, & \text{otherwise.} \end{cases}$$
 (38)

In periporomechanics, with the effective force concept the failure of solid skeleton is modeled through a scalar damage variable φ that tracks the progressive failure of unsaturated porous media. This damage variable is defined as the fraction of broken solid bonds at a material point in its horizon

$$\varphi = 1 - \frac{\int_{\mathcal{H}} \varrho \underline{\omega} \, \mathrm{d}V'}{\omega_0},\tag{39}$$

where $\varphi \in [0, 1]$ and ω_0 is defined by (8). It is hypothesized that once a solid bond breaks it will not sustain any mechanical load and the load at a material point will redistribute to unbroken bonds. If enough bonds break (i.e., $\varphi >= \varphi_{cr}$) and coalesce into a surface, a fracture will form and propagate naturally. In this study, we assume that cracks can be identified if $\varphi \ge 0.5$.

The critical energy per unit fracture area, G_c , can be determined from ϖ_{cr} through a spherical coordinate system as sketched in Figure 3. Referring to Figure 3, the energy per unit fracture area G_c for completely separating the body into two halves reads

$$G_{c} = \int_{0}^{\delta} \int_{0}^{2\pi} \int_{z}^{\delta} \int_{0}^{\Psi} (\varpi_{cr}) \underline{x}^{2} \sin \overline{\alpha}_{1} d\overline{\alpha}_{1} d\underline{x} d\overline{\alpha}_{2} dz,$$

$$= \frac{\pi \delta^{4}}{4} \varpi_{cr}, \tag{40}$$

where $\Psi = \cos^{-1}(z/x)$. It follows from (40) that the critical energy density for bond breakage can be written as

$$\varpi_{cr} = \frac{4G_c}{\pi \delta^4}.\tag{41}$$

From linear elastic fracture mechanics³³ for mode I fracture G_c reads

$$G_c = K_I^2 (1 - \nu^2) / E, \tag{42}$$

where E is Young's modulus, ν is Poisson's ratio, and K_I is the fracture toughness of mode I. Then from (42) the critical energy density for mode I fracture can be written as

$$\varpi_{cr} = \frac{4K_I^2}{\pi E \delta^4} (1 - v^2). \tag{43}$$

It follows from (43) that the critical energy density for bond breakage can be a material property of solid phase. Following the above lines, the critical energy density can be determined for modes II and III fracture.

We assume that a fractured space is formed between two adjacent material points x and x' if both $\varpi \ge \varpi_{cr}$ as well as $\varphi \ge \varphi_{cr}$ and $\varphi' \ge \varphi_{cr}$ at x and x', respectively. Both the material points are defined as the fracture mixed points that represent both the bulk and fractured space. It is further assumed that the fracture mixed point has two fluid pressure degrees of freedom, that is, the bulk fluid pressure and fracture fluid pressure, which will be used to model unsaturated fluid flow in fractured space in Section 2.2.3. Figure 4 draws the kinematics of a bond across the fracture. The relative displacement vector $\eta = u' - u$ can be decomposed into two components as sketched in Figure 4. The two components can be assumed to represent the opening displacement and the dislocation of the crack, respectively. To determine the crack width, we define c as the crack aperture related to the opening displacement as proposed in Reference 44,

$$\underline{c} = y \cos \psi - \underline{x},\tag{44}$$

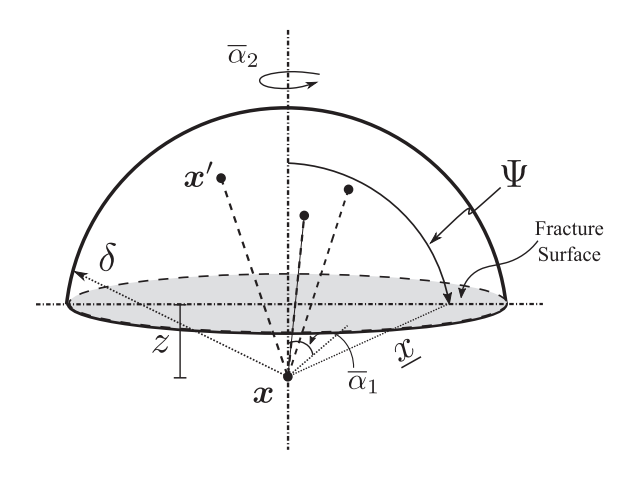


FIGURE 3 Schematic representation of the spherical coordinate system for the evaluation of the energy per unit fracture area G_c for complete separation of two halves of a porous material body (adapted from Reference 34)

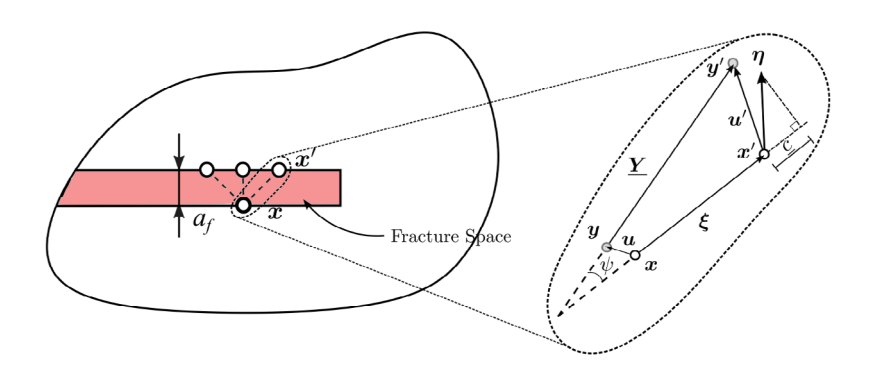


FIGURE 4 Schematic representation of the kinematics of a bond across fracture

where ψ is defined in Figure 4. Therefore, the crack width at fracture point x can be approximated by the average of bond apertures of all broken bonds

$$a_f = \frac{\int_{\mathcal{H}} \overline{\varrho} \underline{c} dV'}{\int_{\mathcal{H}} \overline{\varrho} dV'}, \tag{45}$$

where $\overline{\varrho} = 1 - \varrho$.

Next, we present the equations of motion and mass balance of fracturing unsaturated porous media.

2.2.2 | Equation of motion

In unsaturated periporomechanics, through the effective force concept the same equation of motion is applied on and off the crack surface or crack tip of the solid skeleton in unsaturated porous media. This is an advantage for modeling fracture in unsaturated porous media. For the fully coupled processes of solid deformation and unsaturated fluid flow the equation of motion of a fracture point is different from that of a bulk material point at the constitutive model level. For a bulk material point, the equation of motion can be written by (1). To incorporate bond breakage at a bulk material point x, the effective force state and fluid force state along ξ are written as, respectively

$$\underline{\overline{T}} = \varrho \underline{\omega} \left(\overline{P} K^{-1} \xi + \frac{GC}{\omega_0} \underline{\mathscr{R}}^s \right), \tag{46}$$

$$\overline{\underline{T}}_{w} = -\underline{\omega} P_{w} \mathbf{K}^{-1} \boldsymbol{\xi},\tag{47}$$

where

$$P_w = J p_w \mathbf{1} \widetilde{\boldsymbol{F}}^{-T}. \tag{48}$$

It follows from (46) and (47) that the total force state along a broken bond is

$$\underline{T} = -\underline{\omega} S_r P_w \mathbf{K}^{-1} \boldsymbol{\xi}. \tag{49}$$

The broken bonds are eliminated through $\underline{\rho}$ at the constitutive model level (e.g., the nonlocal deformation gradient and the effective force state). As assumed, along a broken bond the effective force state vanishes. The total force state only consists of the fluid force state that can be written as

$$\underline{\underline{T}}_{w} = -\frac{3\underline{\omega}}{m_{v}} p_{w} \frac{\underline{\underline{Y}}}{\underline{y}},\tag{50}$$

where the ordinary fluid force state is used on broken bonds for simplicity.

For a fracture point, similar to (1) the equation of motion can be written as

$$\rho \ddot{\boldsymbol{u}} = \int_{\mathcal{H}} \left(\overline{\underline{\boldsymbol{T}}} - \overline{\underline{\boldsymbol{T}}}' \right) \, \mathrm{d}V' - \int_{\mathcal{H}} \left(S_l \underline{\boldsymbol{T}}_l - S_l' \underline{\boldsymbol{T}}_l' \right) \, \mathrm{d}V' + \rho \boldsymbol{g}, \tag{51}$$

where

$$S_{l}\underline{T}_{l} = \begin{cases} S_{rf}\underline{T}_{f}, & \text{if } \varphi \& \varphi' \geq \varphi_{cr}, \\ S_{r}\underline{T}_{w}, & \text{otherwise.} \end{cases}$$
(52)

In (52), \underline{T}_f is the fluid force state between two fracture points x and x'

$$\underline{T}_f = -\frac{3\omega}{m_v} p_f \frac{\underline{Y}}{\underline{y}},\tag{53}$$

where p_f and $S_{r,f}$ are fracture fluid pressure and degree of saturation, respectively, at fracture point x.

2.2.3 | Balance of mass

The balance of mass in the continuous porous space (Figure 6A) can be written by (3) at both bulk and fracture material points. In (3), the broken bond (i.e., $\underline{\rho} = 0$) associated with \boldsymbol{x} will not be considered in the second and third terms and at the constitutive model level by multiplying $\underline{\omega}$ by $\underline{\rho}$. For instance, Equations (35) and (36) can be rewritten as

$$\widetilde{\nabla \Phi} = \frac{3}{m_{\nu}} \int_{\mathcal{H}} \underline{\rho} \underline{\omega} \, \underline{\Phi} \xi \, dV', \tag{54}$$

$$\underline{Q} = \frac{3}{m_{\nu}} \underline{\rho}\underline{\omega} \rho_{\nu} \mathbf{q} \xi. \tag{55}$$

The sink/source term will be null for a bulk material point. For a fracture material point, the sink/source term in (3) can be determined assuming that the fluid flow from the pore space into the fracture space follows the generalized Darcy's law for unsaturated fluid flow along the direction normal to the fracture surface. ^{13,41} It follows from this assumption that sink/source term Q_s for the fluid flow from the bulk into the fracture at x can be written as

$$Q_s = A \left[-\frac{k^r k_w}{\mu_w} \left(\frac{p_f - p_w}{l_x} \right) \right] / V, \tag{56}$$

where p_w and p_f are water pressures in the bulk and fracture space respectively, A and V are the cross-sectional area and volume of a material point assuming uniform spatial discretization, $l_x = d/2$ and d is the edge dimension of a cubic material point. Given the source term, following the formulation for unsaturated fluid flow in porous space the mass balance equation of unsaturated fluid flow in fracture space can be written as

$$\frac{\partial S_{r,f}}{\partial t} + \frac{1}{\rho_w} \int_{\mathcal{H}} \left(\underline{Q}_f - \underline{Q}_f' \right) dV' - Q_s = 0, \tag{57}$$

where \underline{Q}_f and \underline{Q}_f' are the fluid flow states at fracture points \boldsymbol{x} and \boldsymbol{x}' , respectively, S_{rf} is the degree of saturation in fracture space that can be determined by the soil–water retention curve in (17). In (57), it is assumed that in fracture space $\phi = 1$ and the volume coupling term vanishes.¹³ \underline{Q}_f is determined by (36) as

$$\underline{Q}_f = \frac{3}{m_v} \underline{\omega} \rho_w \mathbf{q}_f \boldsymbol{\xi},\tag{58}$$

where q_f is the fluid flow vector in fracture space. Through Darcy's law for unsaturated fluid flow^{3,23} the fracture fluid flow vector q_f can be written as

$$\mathbf{q}_f = -\frac{k_f^r k_f}{\mu_w} \widetilde{\mathbf{\nabla}} \widetilde{\Phi}_f, \tag{59}$$

where k_f^r is the relative permeability, k_f is the intrinsic permeability of fracture space, and $\widetilde{\nabla \Phi_f}$ is the nonlocal fracture fluid pressure gradient.

$$k_f^r = S_{r,f}^{1/2} \left[1 - (1 - S_{r,f}^{1/m})^m \right]^2.$$
 (60)

Given the fracture width a_f in (45), k_f can be estimated through the celebrated cubic law (e.g., Reference 13)

$$k_f = \frac{a_f^2}{12}. (61)$$

The nonlocal gradient of fracture fluid pressure can be determined

$$\widetilde{\nabla \Phi_f} = \frac{3}{m_v} \int_{\mathcal{H}} \underline{\omega} \, \underline{\Phi_f} \xi \, dV', \tag{62}$$

where

$$\underline{\Phi}_f = p_f' - p_f, \tag{63}$$

and p_f and p_f' are fracture fluid pressures at fracture points x and x', respectively.

In summary, in the proposed fracturing unsaturated periporomechanics the fundamental unknowns are displacement and fluid pressures in the bulk and fracture space. For a bulk material point, the governing equations consist of the equation of motion and the mass balance equation, that is, (1) and (3). For a fracture material point, the governing equations are the equation of motion, the mass balance equation in the bulk, and the mass balance equation of fluid flow in fracture space, that is, (51), (3), and (57). For boundary conditions, the fictitious boundary layer/volume method is adopted to apply essential boundary conditions (i.e., displacement and pore fluid pressure) and natural boundary conditions (i.e., effective force and fluid flux) (see References 22-24 and 28). We refer to the literature for alternative methods of imposing boundary conditions in peridynamics (e.g., References 56 and 71). In the following section, we present an implicit fractional step algorithm to solve the coupled governing equations of fracturing unsaturated periporomechanics.

3 | NUMERICAL IMPLEMENTATION

3.1 | Fractional step method

The formulated unsaturated fracturing periporomechanics is numerically implemented through the fractional step/staggered algorithm with a two-stage undrained operator split^{25,26,57,59} and mixed meshfree method.²⁴ The two-stage operator split converts the coupled fracturing periporomechanics problem into an undrained mechanical problem and an unsaturated fluid flow problem in the deformed solid configuration. We note that the drained operator split that involves

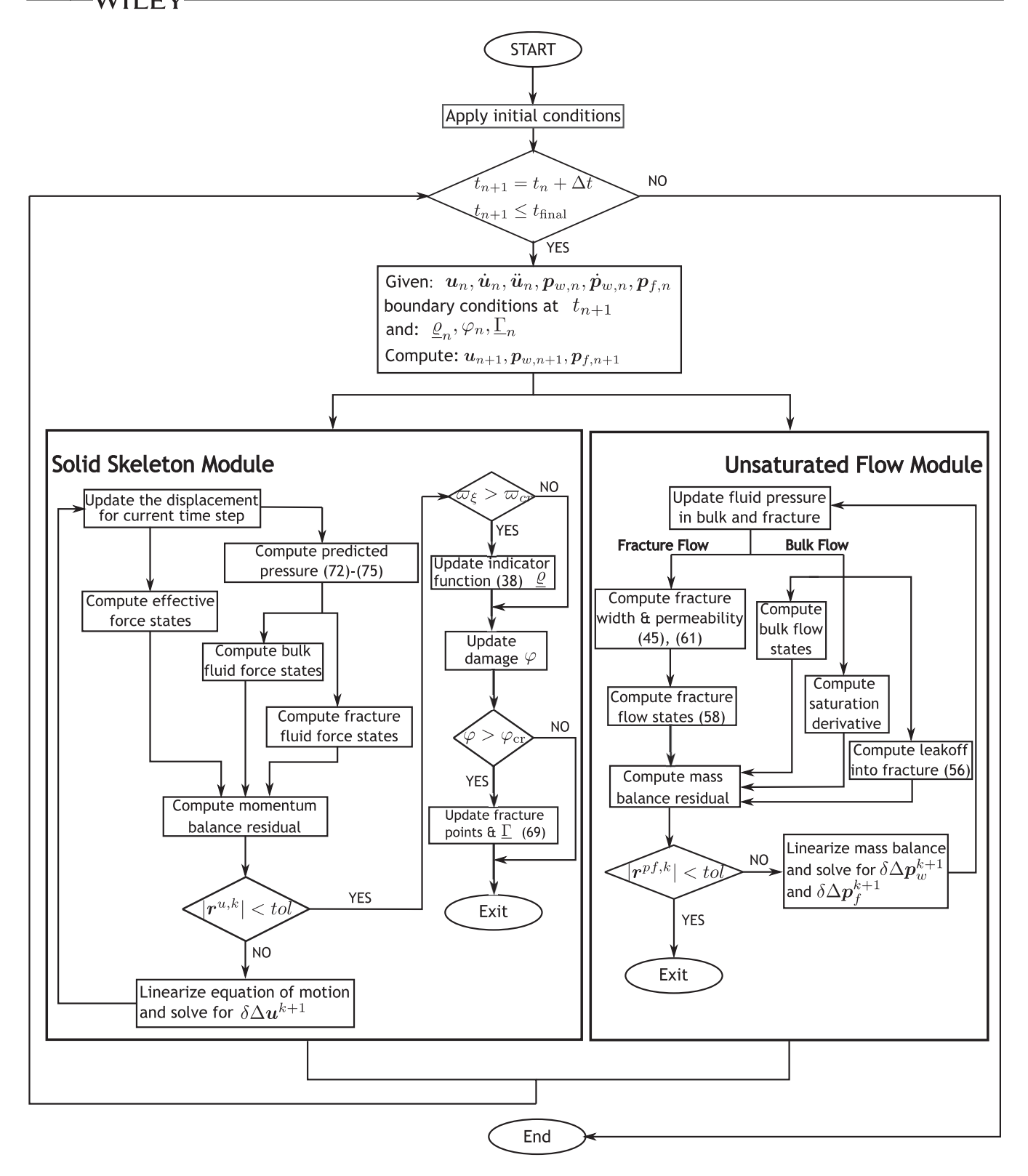


FIGURE 5 Flowchart for the implicit fractional step algorithm for fracturing unsaturated periporomechanics

simply freezing the fluid pressure during the mechanical stage is only conditionally stable.^{58,72} The undrained operator split preserves the contractivity of the original coupled problem and is unconditionally stable.⁵⁹ It is noted that both monolithic and staggered approaches can be exploited to solve the fracturing unsaturated periporomechanics model in this study. In the monolithic approach, the full system of coupled algebraic equations is solved simultaneously at each time step. With an implicit time integration scheme, it is unconditionally stable and preserves the strong physical

Algorithm 1. Global fractional-step time integration scheme for fracturing porous media

```
1: procedure GIVEN \boldsymbol{u}_n, \boldsymbol{p}_{w,n}, \boldsymbol{p}_{f,n}, t_n and \Delta t, Compute \boldsymbol{u}, \boldsymbol{p}_w and \boldsymbol{p}_f
           t = t_n + \Delta t
 2:
           while t \le t_{\text{final}} do
 3:
                 Apply boundary conditions
 4:
                 Compute the effective force and fluid force via Algorithm 2.
 5:
                 Compute the balance of momentum residual \mathcal{R}^{u,0}
 6:
                 Set k = 0 and tol = 10^{-6}
 7.
                 if |\mathcal{R}^{u,0}| > tol then
 8:
                       while |\mathcal{R}^{u,k}|/|\mathcal{R}^{u,0}| > \text{tol do}
 9:
                             Construct the tangent operator for balance of momentum \mathbf{A}^{u,k} = \left[ \partial \mathbf{R}^{u,k} / \partial \Delta \mathbf{u}^k \right]
10:
                             Solve the linear system \mathbf{A}^{u,k}\delta\Delta\mathbf{u}^{k+1} = -\mathbf{R}^{u,k} for \delta\Delta\mathbf{u}^{k+1}
11:
                             Update u^{k+1}, \dot{u}^{k+1} and \ddot{u}^{k+1} using (64), (65), and (66)
12:
                             Update the effective force and fluid force via Algorithm 2
13:
                             Update the residual \mathcal{R}^{u,k+1}
14:
                             Set k \leftarrow k + 1
15:
                       end while
16:
                 end if
17.
                 Update the list of broken bonds and fracture points via Algorithm 3
18:
                 Compute the fluid flow in the bulk and fracture via Algorithm 4
19:
                 Compute the balance of mass residual \mathcal{R}^{pf,0} = {\mathcal{R}^{p,0}; \mathcal{R}^{f,0}}
20.
21:
                 if |\mathcal{R}^{pf,0}| >tol then
22:
                       while |\mathcal{R}^{pf,k}|/|\mathcal{R}^{pf,0}| > tol do
23.
                             Construct the tangent \mathbf{A}^{pf,k} = \left[ \{ \partial \mathbf{R}^{pf,k} / \partial \Delta \mathbf{p}_w^k \}, \{ \partial \mathbf{R}^{pf,k} / \partial \Delta \mathbf{p}_f^k \} \right]
24:
                             Solve the linear system \mathcal{A}^{pf,k} \{\delta \Delta \mathbf{p}_w; \delta \Delta \mathbf{p}_f\}^{k+1} = -\{\mathcal{R}^p; \mathcal{R}^f\}^k \text{ for } \{\delta \Delta \mathbf{p}_w; \delta \Delta \mathbf{p}_f\}^{k+1}
25:
                             Update \boldsymbol{p}_{w}^{k+1} and \boldsymbol{p}_{f}^{k+1} using (81) and (82)
26:
                             Update the fluid flow in the bulk and fracture via Algorithm 4
27:
                             Update the residual \mathcal{R}^{pf,k+1}
28:
                             Set k \leftarrow k+1
29:
                       end while
30:
31:
                 end if
                 Update \boldsymbol{u}_n \leftarrow \boldsymbol{u}, \boldsymbol{p}_{w,n} \leftarrow \boldsymbol{p}_w, \boldsymbol{p}_{f,n} \leftarrow \boldsymbol{p}_f
32:
            end while
33:
34: end procedure
```

coupling between the phases. However, it can lead to large complex systems that may be asymmetric and cannot leverage the different phenomenological time scales of individual phases.²⁵ We refer to the distinguished literature (e.g., References 25 and 26) for an in-depth discussion of the monolithic and fractional step/staggered algorithms for numerically implementing coupled multiphysics frameworks for porous media.

Figure 5 provides a flowchart of the proposed implicit fractional step algorithm, and Algorithm 1 presents a detailed step-by-step procedure.

3.1.1 | Time discretization of the equation of motion under undrained condition

In the mechanical stage, the equation of motion will be solved first under undrained condition through Newton's method.

At time step n, u_n , \dot{u}_n , \ddot{u}_n are known. Let $\Delta u_{n+1} = u_{n+1} - u_n$, in line with Newmark's method⁷³ the displacement, velocity, and acceleration of the solid skeleton at time step n + 1 can be written as

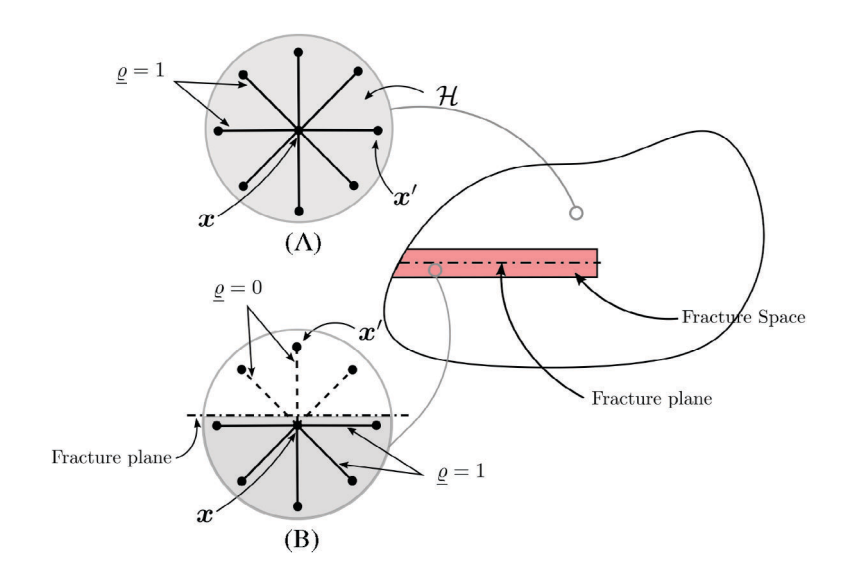


FIGURE 6 Schematic representation of (A) a point in the bulk and (B) a fracture point adjacent to the crack

Algorithm 2. Compute the effective force and fluid force

```
1: procedure Given u^k, \dot{u}^k, \ddot{u}^k, \varrho_n, \underline{\Gamma}_n Construct effective force vector \mathcal{F}^k and fluid force vector \overline{\mathcal{F}^k_w}
 2:
         for all points do
              Compute weighted volume m_v and shape tensor K
 3:
              Compute deformation gradient \tilde{F}^k using (12)
 4:
              Compute effective Piola-Kirchhoff stress \overrightarrow{P} using constitutive model
 5:
              Compute volume coupling term \mathcal{V}^k using (100)
 6:
              Compute force states \underline{\underline{T}}^k, \underline{\underline{T}}_w^k and \underline{\underline{T}}_f^k using (46), (47), and (53)
 7:
              Compute bulk fluid pressure rate \widetilde{p}_w^k using (72)
 8:
              Compute fracture fluid pressure rate \hat{p}_f^k using (73)
 9:
              Compute bulk fluid pressure \widetilde{p}_{w}^{k} using (74) and fracture fluid pressure \widetilde{p}_{f}^{k} using (75)
10:
              Compute effective force vector \mathcal{T}^k using (94)
11:
              Compute fluid force vector \mathcal{T}_w^k using (95)
12:
         end for
13:
14: end procedure
```

$$\mathbf{u}_{n+1} = \mathbf{u}_n + \Delta \mathbf{u}_{n+1},\tag{64}$$

$$\dot{\boldsymbol{u}}_{n+1} = \frac{2\beta_2}{\beta_1 \Delta t} \Delta \boldsymbol{u}_{n+1} - \left(\frac{2\beta_2}{\beta_1} - 1\right) \dot{\boldsymbol{u}}_n - \Delta t \left(\frac{\beta_2}{\beta_1} - 1\right) \ddot{\boldsymbol{u}}_n, \tag{65}$$

$$\ddot{\boldsymbol{u}}_{n+1} = \frac{2}{\beta_1 \Delta t^2} \Delta \boldsymbol{u}_{n+1} - \frac{2}{\beta_1 \Delta t} \dot{\boldsymbol{u}}_n - \left(\frac{1}{\beta_1} - 1\right) \ddot{\boldsymbol{u}}_n,\tag{66}$$

where β_1 and β_2 are numerical integration parameters. For unconditional stability, $\beta_1 \geq \beta_2 \geq 0.5$.

Figure 6 presents a schematic of (a) a material point in the bulk and (b) a material point adjacent to the fracture. At t_{n+1} , the residual of the equation of motion at a bulk point reads

$$\mathbf{r}_{n+1}^{\mu} = \rho \ddot{\mathbf{u}} - \int_{\mathcal{H}} \underline{\rho}_{n} \left(\overline{\underline{\mathbf{T}}} - \overline{\underline{\mathbf{T}}}' \right) dV' + \int_{\mathcal{H}} \left(S_{r} \underline{\mathbf{T}}_{w} - S_{r}' \underline{\mathbf{T}}_{w}' \right) dV' - \rho \mathbf{g}.$$
 (67)

For a fracture point, the residual of the equation of motion (from 51) is expressed as

$$\mathbf{r}_{n+1}^{\mu} = \rho \ddot{\mathbf{u}} - \int_{\mathcal{H}} \underline{\rho}_{n} \left(\overline{\underline{\mathbf{T}}} - \overline{\underline{\mathbf{T}}}' \right) dV' + \int_{\mathcal{H}} (1 - \underline{\Gamma}_{n}) \left(S_{w} \underline{\mathbf{T}}_{w} - S'_{w} \underline{\mathbf{T}}'_{w} \right) dV' + \int_{\mathcal{H}} \underline{\Gamma}_{n} \left(S_{f} \underline{\mathbf{T}}_{f} - S'_{f} \underline{\mathbf{T}}'_{f} \right) dV' - \rho \mathbf{g}, \tag{68}$$

where

$$\underline{\Gamma}_n = \begin{cases} 1, & \text{if } \mathbf{x} \& \mathbf{x'} \text{ are fracture points at } t_n, \\ 0, & \text{otherwise.} \end{cases}$$
 (69)

We note that in (67) and (68) the subscript n+1 of variables at time step n+1 is omitted for brevity. This notation is followed in the remaining section unless otherwise for clarity. The fluid pressure terms in (67) and (68) are determined from the explicit fluid pressure predictors under undrained condition that are defined in what follows. At time step n, $p_{w,n}$ and $p_{f,n}$, and their rate forms, $\dot{p}_{w,n}$ and $\dot{p}_{f,n}$ are known. Let $\tilde{p}_{w,n+1}$ and $\tilde{p}_{f,n+1}$ be the explicit fluid pressure predictors at time step n+1 under undrained condition. It follows from Newmark's method^{24,26} that the rate forms of $\tilde{p}_{w,n+1}$ and $\tilde{p}_{f,n+1}$ can be written as

$$\dot{\widetilde{p}}_{w,n+1} = \frac{1}{\beta_3 \Delta t} \Delta \widetilde{p}_{w,n+1} - \left(\frac{1}{\beta_3} - 1\right) \dot{p}_{w,n},\tag{70}$$

$$\dot{\widetilde{p}}_{f,n+1} = \frac{1}{\beta_3 \Delta t} \Delta \widetilde{p}_{f,n+1} - \left(\frac{1}{\beta_3} - 1\right) \dot{p}_{f,n},\tag{71}$$

where $\Delta \widetilde{p}_{w,n+1} = \widetilde{p}_{w,n+1} - p_{w,n}$ and $\Delta \widetilde{p}_{f,n+1} = \widetilde{p}_{fn+1} - p_{f,n}$, and β_3 is an integration parameter ($\beta_3 \ge 0.5$ for unconditional stability). Under undrained condition, $\widetilde{p}_{w,n+1}$ and $\widetilde{p}_{f,n+1}$ can be determined from the mass balance equations of unsaturated fluid flow in the bulk and fracture as follows.

$$\dot{\widetilde{p}}_{w,n+1} = -\left(\phi \frac{\partial S_{r,n}}{\partial p_{w,n}}\right)^{-1} \left[S_{r,n} \int_{\mathcal{H}} \underline{\varrho}_n \left(\underline{\dot{\mathcal{V}}} - \underline{\dot{\mathcal{V}}}'\right) dV' + \frac{1}{\rho_w} \int_{\mathcal{H}} \underline{\varrho}_n \left(\underline{Q} - \underline{Q}'\right)_n dV' + Q_{s,n}\right],\tag{72}$$

$$\dot{\widetilde{p}}_{f,n+1} = -\left(\frac{\partial S_{r,f}}{\partial p_f}\right)_n^{-1} \left[\frac{1}{\rho_w} \int_{\mathcal{H}} \underline{\Gamma}_n \left(\underline{Q}_f - \underline{Q}_f'\right)_n \, dV' - \mathcal{Q}_{s,n}\right] \\
= \dot{p}_{f,n}. \tag{73}$$

We note that $Q_{s,n} = 0$ in (72) at a mixed point in the bulk. Thus, (72) represents the rates of water pressure predictors at the bulk and fracture points. Then, it follows from (70)–(73) that the explicit fluid pressure predictors can be written as

$$\tilde{p}_{w,n+1} = \beta_3 \Delta t \dot{\tilde{p}}_{w,n+1} + (1 - \beta_3) \Delta t \dot{p}_{w,n} + p_{w,n}, \tag{74}$$

$$\widetilde{p}_{f,n+1} = \beta_3 \Delta t \widetilde{p}_{f,n+1} + (1 - \beta_3) \Delta t \dot{p}_{f,n} + p_{f,n}
= \Delta t \dot{p}_{f,n} + p_{f,n}.$$
(75)

The fluid pressure predictors from (74) and (75) are then used to determine the fluid force states in (67) and (68). Substituting (64)–(66) into (67) and (68) and using (74) and (75), Δu_{n+1} can be solved by Newton's method in what follows (see Algorithm 2). Let k be the iteration number

$$\mathbf{R}^{u,k+1} = \mathbf{R}^{u,k} + A^{u,k} \delta \Delta \mathbf{u}^{k+1} \approx \mathbf{0}. \tag{76}$$

where \mathcal{R}^u is the global residual vector of (68) and \mathcal{A}^u is the global tangent operator that is defined as

$$\mathcal{A}^{u,k} = \frac{\partial \mathcal{R}^{u,k}}{\partial \Delta u^k}.\tag{77}$$

Solving (76) we obtain

$$\delta \Delta \boldsymbol{u}^{k+1} = -(\boldsymbol{\mathcal{A}}^k)^{-1} \boldsymbol{\mathcal{R}}^{u,k}. \tag{78}$$

Finally, we have

$$\Delta \mathbf{u}^{k+1} = \Delta \mathbf{u}^k + \delta \Delta \mathbf{u}^{k+1}. \tag{79}$$

At the end of the mechanical stage, the broken bonds and indicator functions (i.e., 69) are updated following Algorithm 3. The energy dissipation of individual bonds is written as

$$\underline{\underline{w}}_{n+1} = \underline{\underline{w}}_n + \left(\underline{\overline{T}} - \underline{\overline{T}}'\right)_{n+1} \Delta \eta$$

$$= \underline{\underline{w}}_n + \left(\underline{\overline{T}} - \underline{\overline{T}}'\right)_{n+1} (\Delta u' - \Delta u). \tag{80}$$

The database of damaged bonds is updated for bonds with $\underline{\varpi} > \varpi_{cr}$ via (38) and then φ is updated at each material point. Using φ , the database of fracture points is updated.

Algorithm 3. Update the database of broken bonds and fracture points

```
1: oldsymbol{procedure} Given \overline{\underline{T}} and \Delta oldsymbol{\eta} Update indicator arrho and damage variable arphi
 2:
        for all points do
             for each neighbor do
 3:
                 Compute bond energy \varpi using (80)
 4:
                 if \varpi > \varpi_{cr} then
 5:
                     Update \rho using (38) to reflect bond damage status
 6:
                     Update damage variable \varphi using (39)
 7:
                     Sum the energy in the bond into the total energy dissipated at the point
 8:
                 end if
 9.
             end for
10:
             if \varphi \geq \varphi_{cr} then
11:
12:
                 set material point x as fracture point
13:
        end for
14:
15: end procedure
```

The solution of the mechanical stage and the rate forms of the fluid pressure predictors at time t_{n+1} from the mechanical solver are passed to the unsaturated fluid flow solver for the fluid flow stage at time step t_{n+1} .

3.1.2 | Time discretization of the mass balance equation in the deformed configuration

Given $p_{w,n}$, $p_{f,n}$, $\dot{p}_{w,n}$, $\dot{p}_{f,n}$, and $\dot{\boldsymbol{u}}_{n+1}$, the unsaturated fluid flow stage solves $p_{w,n+1}$ and $p_{f,n+1}$ in the updated solid configuration (i.e., \boldsymbol{u}_{n+1}) at t_{n+1} using Newton's method. Let $\Delta p_{w,n+1} = p_{w,n+1} - p_{w,n}$ and $\Delta p_{f,n+1} = p_{f,n+1} - p_{f,n}$. It follows from Newmark's method⁷³ that

$$p_{w,n+1} = p_{w,n} + \Delta p_{w,n+1},\tag{81}$$

$$p_{f,n+1} = p_{f,n} + \Delta p_{f,n+1}, \tag{82}$$

$$\dot{p}_{w,n+1} = \frac{1}{\beta_3 \Delta t} \Delta p_{w,n+1} - \left(\frac{1}{\beta_3} - 1\right) \dot{p}_{w,n},\tag{83}$$

$$\dot{p}_{f,n+1} = \frac{1}{\beta_3 \Delta t} \Delta p_{f,n+1} - \left(\frac{1}{\beta_3} - 1\right) \dot{p}_{f,n}. \tag{84}$$

At t_{n+1} , the residuals of the mass balance equations can be written as

$$r_{n+1}^{p} = \phi \left(\frac{\partial S_r}{\partial p_w} \right) \dot{p}_w + \frac{1}{\rho_w} \int_{\mathcal{H}} \underline{\varrho} \left(\underline{Q} - \underline{Q}' \right) dV' + S_r^k \int_{\mathcal{H}} \underline{\varrho} \left(\underline{\dot{V}} - \underline{\dot{V}}' \right) dV' + \mathcal{Q}_s, \tag{85}$$

$$r_{n+1}^{f} = \left(\frac{\partial S_{r,f}}{\partial p_{f}}\right) \dot{p}_{f} + \frac{1}{\rho_{w}} \int_{\mathcal{H}} \underline{\Gamma}\left(\underline{Q}_{f} - \underline{Q}_{f}'\right) dV' - Q_{s}. \tag{86}$$

Algorithm 4. Compute the unsaturated fluid flow in the bulk and fracture

```
1: procedure Given p_w^k, p_f^k, \dot{u}, \varrho, \Gamma Construct bulk fluid flow \mathcal{Q}^k and fracture flow \mathcal{Q}_f^k
 2:
        for all points do
            Compute pressure potential states \Phi^k
 3:
            Compute weighted volume m_{\nu} and shape tensor K
 4:
            Compute pressure gradient \widetilde{\nabla \Phi}^k using (15)
 5:
            Compute relative permeability k^{r,k} using (18)
 6:
            Compute flux vector \mathbf{q}^k using (15)
 7:
            Compute flow states Q^k using (14)
 8:
            Compute bulk fluid flow Q^k using (99)
 9:
        end for
10:
        for all fracture points do
11:
            Compute fracture width a_f using (45)
12:
            Compute fracture permeability k_f using (61)
13:
            Compute Q_s^k using (56)
14:
            for each neighboring fracture point do
15:
                 Compute fracture pressure states \Phi_f^k using (63)
16:
                Compute fracture pressure gradient \widetilde{\nabla \Phi_f}^k and fracture flux \boldsymbol{q}_f^k using (62) and (59)
17:
                Compute fracture flow states \underline{Q}_f^k using (58)
18:
19:
            Compute fracture flow \mathcal{Q}_f^k using (103) and source term \mathcal{Q}_s^k using (101)
20:
        end for
21:
22: end procedure
```

Substituting (81)–(84) into (85) and (86), $\Delta p_{w,n+1}$ and $\Delta p_{f,n+1}$ can be solved by Newton's method in what follows (see Algorithm 4 for details). Again, let k be the iteration number

$$\begin{Bmatrix} \mathbf{\mathcal{R}}^{p,k+1} \\ \mathbf{\mathcal{R}}^{f,k+1} \end{Bmatrix} = \begin{Bmatrix} \mathbf{\mathcal{R}}^{p,k} \\ \mathbf{\mathcal{R}}^{f,k} \end{Bmatrix} + \mathbf{\mathcal{A}}^{pf,k} \begin{Bmatrix} \delta \Delta \mathbf{p}_w^{k+1} \\ \delta \Delta \mathbf{p}_f^{k+1} \end{Bmatrix} \approx \mathbf{0},$$
(87)

where \mathcal{R}^p and \mathcal{R}^f are the global residual vectors of the mass balance equations of the bulk and fracture, respectively, $\Delta \boldsymbol{p}_w$ and $\Delta \boldsymbol{p}_f$ are the global fluid pressure increments in the bulk and fracture, respectively, and \mathcal{A}^{pf} is the coupled tangent operator of the mass balance equations

$$\mathcal{A}^{pf,k} = \begin{cases} \frac{\partial \mathcal{R}^{p,k}}{\partial \Delta \mathbf{p}_{w}^{k}} & \frac{\partial \mathcal{R}^{p,k}}{\partial \Delta \mathbf{p}_{f}^{k}} \\ \frac{\partial \mathcal{R}^{f,k}}{\partial \Delta \mathbf{p}_{w}^{k}} & \frac{\partial \mathcal{R}^{f,k}}{\partial \Delta \mathbf{p}_{f}^{k}} \end{cases} . \tag{88}$$

Solving (87) gives

$$\begin{cases}
\delta \Delta \boldsymbol{p}_{w}^{k+1} \\
\delta \Delta \boldsymbol{p}_{f}^{k+1}
\end{cases} = -(\boldsymbol{\mathcal{A}}^{pf,k})^{-1} \left\{ \boldsymbol{\mathcal{R}}^{p,k} \\ \boldsymbol{\mathcal{R}}^{f,k} \right\}.$$
(89)

It is noted that $\dot{\tilde{p}}_{w,n+1}$ and $\dot{\tilde{p}}_{f,n+1}$ from the undrained mechanical stage are used as the initial values of $\dot{p}_{w,n+1}$ and $\dot{p}_{f,n+1}$ (i.e., k=0). Finally, we have

$$\Delta \boldsymbol{p}_{w}^{k+1} = \Delta \boldsymbol{p}_{w}^{k} + \delta \Delta \boldsymbol{p}_{w}^{k+1}, \tag{90}$$

$$\Delta \mathbf{p}_f^{k+1} = \Delta \mathbf{p}_f^k + \delta \Delta \mathbf{p}_f^{k+1}. \tag{91}$$

3.2 | Mixed meshfree spatial discretization

The formulated fracture periporomechanics model is discretized in space by a mixed Lagrangian–Eulerian meshfree scheme.²⁴ The uniform mixed material points are used in this study. Let \mathcal{N}_i be the number of mixed material points in the horizon of a mixed material point i, \mathcal{P} be the number of total mixed material points in the problem domain, and \mathcal{A} be the assembly operator.²⁴

3.2.1 | Spatial discretization of the equation of motion

It follows from (67) and (68) that the global residual vector of the equation of motion \mathcal{R}^u at time step n+1 can be constructed as²⁴

$$\mathcal{R}_{n+1}^{u} = \mathcal{A}_{i=1}^{P} \left(\mathcal{M}_{i} + \mathcal{T}_{s,i} - \mathcal{T}_{w,i} \right), \tag{92}$$

where \mathcal{M}_i , $\mathcal{T}_{s,i}$, and $\mathcal{T}_{w,i}$ are the inertial and gravity load, the effective force, and the fluid force at the mixed material point i.

$$\mathcal{M}_i = \left[\rho_s (1 - \phi_i) + \rho_w S_{r,i} \phi_i \right] (\ddot{\boldsymbol{u}}_i - \boldsymbol{g}) V_i, \tag{93}$$

$$\mathcal{F}_{s,i} = \sum_{i=1}^{N_i} \underline{\varrho}_{ij,n} \left(\overline{\underline{T}}_{ij} - \overline{\underline{T}}_{ji} \right) V_j V_i, \tag{94}$$

$$\mathcal{T}_{w,i} = \sum_{j=1}^{N_i} (1 - \underline{\Gamma}_{ij,n}) \left(S_{r,i} \underline{\boldsymbol{T}}_{w,ij} - S_{r,j} \underline{\boldsymbol{T}}_{w,ji} \right) V_j V_i + \sum_{j=1}^{N_i} \underline{\Gamma}_{ij,n} \left(S_{rf,i} \underline{\boldsymbol{T}}_{f,ij} - S_{rf,j} \underline{\boldsymbol{T}}_{f,ji} \right) V_j V_i, \tag{95}$$

where *j* denotes material points in the horizon of the mixed material point *i*.

3.2.2 | Spatial discretization of the mass balance equation

From (85) and (86), the global residual vectors of the mass balance equations \mathbb{R}^p and \mathbb{R}^f at time step n+1 can be respectively written as

$$\mathcal{R}_{n+1}^{p} = \mathcal{A}_{i=1}^{p} (\mathcal{X}_{i} + \mathcal{Q}_{i} + \mathcal{V}_{i} + \mathcal{Q}_{s,i}), \tag{96}$$

$$\mathcal{R}_{n+1}^{f} = \mathcal{A}_{i=1}^{P_f} (\mathcal{X}_{f,i} + \mathcal{Q}_{f,i} - \mathcal{Q}_{s,i}), \tag{97}$$

where \mathcal{P}_f is the number of fracture points and

$$\mathcal{X}_{i} = -\Delta t \phi_{i} \frac{\partial S_{r,i}}{\partial s_{i}} \dot{p}_{w,i} V_{i}, \tag{98}$$

$$\mathcal{Q}_i = \frac{\Delta t}{\rho_w} \sum_{j=1}^{N_i} \underline{\rho}_{ij,n+1} \left(\underline{Q}_{ij} - \underline{Q}_{ji} \right) V_j V_i, \tag{99}$$

$$\mathcal{V}_{i} = \Delta t S_{r,i} \sum_{j=1}^{\mathcal{N}_{i}} \underline{\varrho}_{ij,n+1} \left(\underline{\dot{\mathcal{V}}}_{ij} - \underline{\dot{\mathcal{V}}}_{ji} \right) V_{j} V_{i}, \tag{100}$$

$$\mathcal{Q}_{s,i} = \Delta t \left[-\frac{k^r k_w}{\mu_w} \left(\frac{p_{f,i} - p_{w,i}}{l_i} \right) \right] A_i, \tag{101}$$

$$\mathcal{X}_{f,i} = -\Delta t \frac{\partial S_{rf,i}}{\partial p_f, i} \dot{p}_{f,i} V_i, \tag{102}$$

$$\mathcal{Q}_{f,i} = \frac{\Delta t}{\rho_w} \sum_{j=1}^{N_i} \underline{\Gamma}_{ij,n+1} \left(\underline{Q}_{f,ij} - \underline{Q}_{f,ji} \right) V_j V_i. \tag{103}$$

4 | NUMERICAL EXAMPLES

4.1 | Example 1: Mode I crack propagation

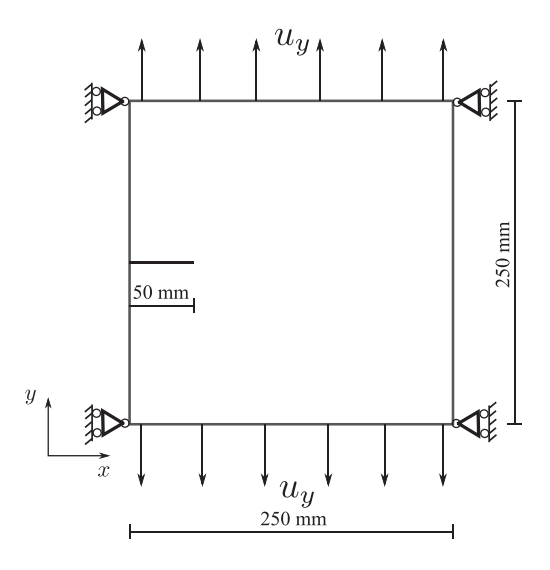
In this example, we simulate mode I crack propagation and unsaturated fluid flow in a porous body under two dimensions. Figure 7 depicts the problem geometry, boundary conditions, and loading protocol. The pre-existing crack is modeled by eliminating interaction between material points across the crack plane. All fluid phase boundaries of the specimen are assumed impermeable. The problem domain is discretized into 20,000 mixed material points with d = 2.5 mm.

The solid phase is modeled using an isotropic elastic correspondence constitutive model. ^{22,23} This applies to all subsequent examples in this section. It is assumed that $\rho_s = 2000 \text{ kg/m}^3$, $\rho_w = 1000 \text{ kg/m}^3$, $\mu_w = 1 \times 10^{-3} \text{ Pa} \text{ s}$, initial porosity $\phi_0 = 0.25$ and $G_c = 95 \text{ J/m}^2$. Unless otherwise noted, these parameters are also used in all subsequent examples. The remaining material parameters in Reference 74 are $K = 13.46 \times 10^6 \text{ kPa}$, $\mu_s = 10.95 \times 10^6 \text{ kPa}$, $k_w = 6 \times 10^{-21} \text{ m}^2$, n = 1.7844, $s_a = 18.6 \times 10^3 \text{ kPa}$. The horizon $\delta = 3.05d$. The stabilization parameter $G = 1.0.^{24}$ As in Reference 74, the specimen is prescribed zero initial effective stress and water pressure. The loading rate $u_y = 2.35 \times 10^{-5} \text{ mm/s}$. The total loading time t = 2000 s with the time increment $\Delta t = 1 \text{ s}$. We investigate the influence of δ and $m = \delta/d$ on the crack propagation and unsaturated fluid flow. The loading curves are compared with the numerical results from the extended finite element method (XFEM) in Reference 74.

4.1.1 | Influence of δ

The horizon δ plays a critical role in modeling the actual behavior of materials using peridynamics. However, its calibration for specific applications is still an open question in peridynamics. To examine the sensitivity of the results to the horizon δ , we run the simulations with three values of horizon, $\delta = 11.3$, 7.5, and 6 mm assuming m = 3. The corresponding spatial discretizations consist of 9000, 20,000, and 36,000 mixed points, respectively. All other parameters are identical. The results are presented in Figures 8–10.

Figure 8 plots the loading curves from the PPM simulations and the result from the XFEM simulation in Reference 74. The results in Figure 8 show that the loading curves from the simulations in this study are consistent with the results from the XFEM method. The loading curve for the simulation with $\delta = 11.3$ mm deviates from the results with $\delta = 7.5$ mm and $\delta = 6$ mm. Recall that the micromechanical modulus C in (7) is an inverse function of the horizon. The smaller peak load of the simulation using $\delta = 11.3$ could be related to C in the stabilization term. Figures 9 and 10 plot the contours of damage variable φ and water pressure at $u_y = 2.5 \times 10^{-2}$ mm, respectively. The results in Figure 9 show that δ could slightly affect the damage zone and crack propagation length. Specifically, the lengths of the new crack are 93, 97, and 98 cm for the simulations with $\delta = 11.3$, 7.5, and 6.0 mm, respectively. Figure 10 shows that the water pressure is negative



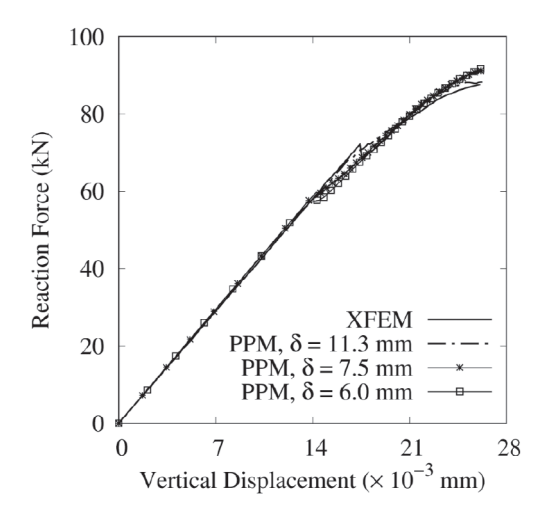


FIGURE 8 Comparison of the loading curves from the simulations using three values of δ and the XFEM result⁷⁴

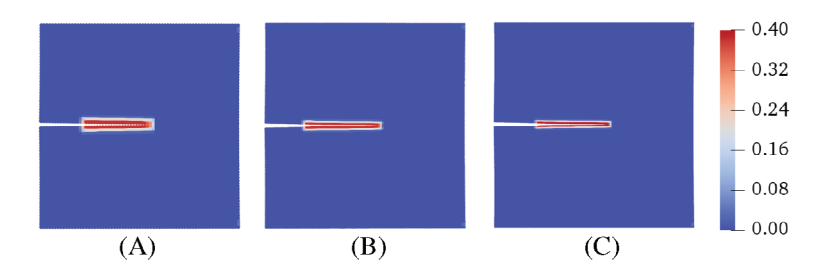


FIGURE 9 Contours of the damage variable φ from the simulations with (A) $\delta = 11.3$ mm, (B) $\delta = 7.5$ mm, and (C) $\delta = 6$ mm, at $u_v = 2.5 \times 10^{-2}$ mm (×50)

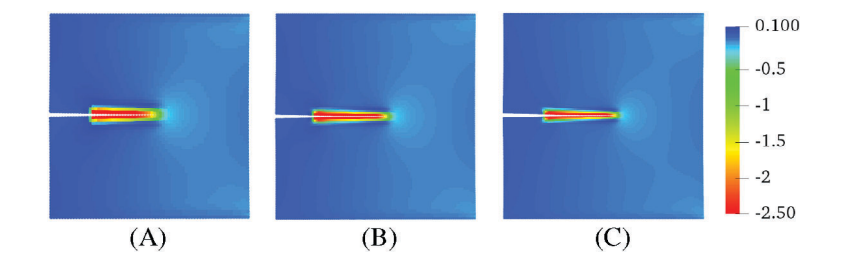


FIGURE 10 Contours of water pressure (MPa) from the simulations with (A) $\delta = 11.3$ mm, (B) $\delta = 7.5$ mm, and (C) $\delta = 6.0$ mm, at $u_v = 2.5 \times 10^{-2}$ mm (×50)

(i.e., matric suction) around the propagated crack for all three cases. Consistent with the results in Figure 9, the value of δ affects the distribution of negative water pressure around the newly formulated crack. The negative water pressure near the new crack can be caused by the competing factors between the crack opening space and the amount of water flowing into the fracture space. Following this reasoning, the negative water pressure could be generated by the crack opening and dilation in the bulk around the crack.

4.1.2 | Influence of m

The ratio $m = \delta/d$ is a measure of the number of mixed points within the horizon of a mixed point. It is another factor that could affect the numerical results with peridynamics. To study the influence of m on the results, we rerun the simulations with m = 2, 3, and 4 and $\delta = 7.5$ mm. The spatial discretizations consist of 9000, 20,000, and 36,000 mixed points, respectively. All other parameters remain the same.

Figure 11 plots the loading curves of the three simulations and the XFEM result.⁷⁴ Figures 12 and 13 compare the contours of damage variable and water pressure, respectively, at $u_y = 2.5 \times 10^{-2}$ mm.

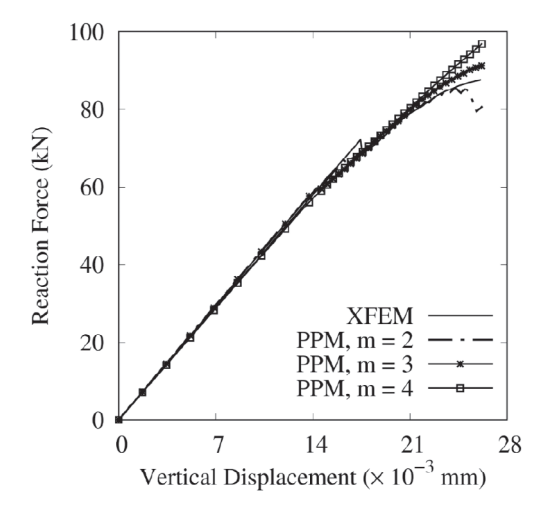


FIGURE 11 Comparison of the loading curves from the PPM simulations using a constant $\delta = 7.5$ mm and three m-ratios and the XFEM result⁷⁴

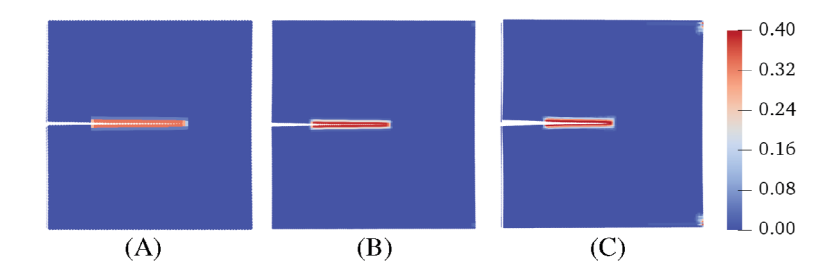


FIGURE 12 Contours of the damage variable φ from the simulations with (A) m = 2, (B) m = 3, and (C) m = 4 at $u_y = 2.5 \times 10^{-2}$ mm (×50)

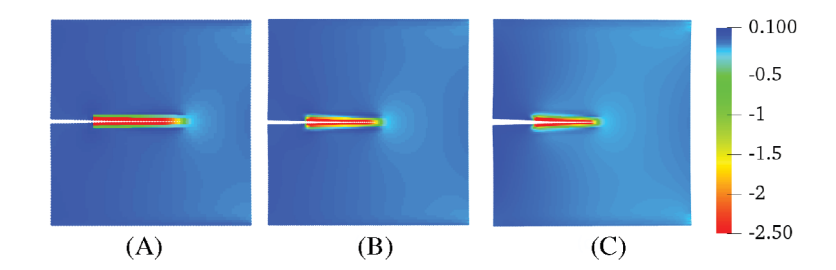


FIGURE 13 Contours of water pressure (MPa) from the simulations with (A) m = 2, (B) m = 3, and (C) m = 4 at $u_y = 2.5 \times 10^{-2}$ mm (×50)

In the early stage, the loading curves in Figure 11 are identical for all simulations. However, the simulations using m=3 and m=4 predict larger peak loads than the XFEM result. As shown in Figure 12A–C, there is a noticeable decrease in crack length from the simulations using larger values of m. For instance, the crack length is 135 mm from m=2 and the crack length is 90 mm from m=4. These differences in crack length are reflected in the force plot (Figure 11), for example, a larger peak load for a larger value of m. It is noted that previous studies conducted using PPM²⁴ or hybrid FEM-PD (peridynamics)^{44,55} have successfully used m=2 to reproduce static and dynamic coupling phenomena in the continuum analysis of porous media. From this example, it appears that m=3 is an appropriate choice when modeling mode I crack propagation in unsaturated porous media.

4.2 | Example 2: Mode II crack propagation

In this example, we model mode II crack propagation by simulating shear loading of a pre-cracked porous body as inspired by an example in Reference 13. We note that the example in Reference 13 was simulated by a saturated poromechanics



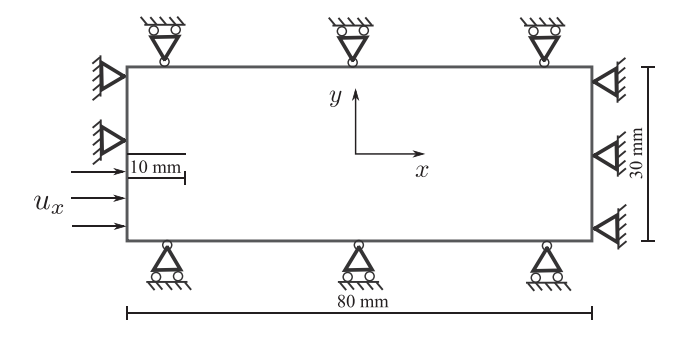


FIGURE 14 Problem setup for Example 2

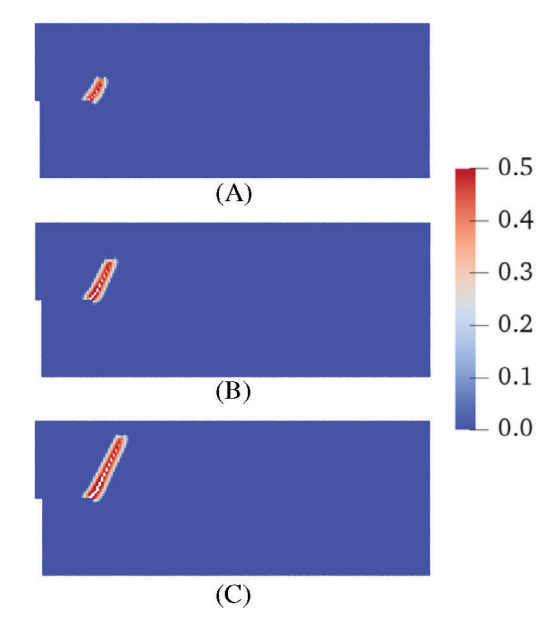


FIGURE 15 Contours of the damage variable φ at (A) $u_x = 2.0 \times 10^{-2}$ mm, (B) $u_x = 2.5 \times 10^{-2}$ mm, and (C) $u_x = 3.0 \times 10^{-2}$ mm (×50)

model. Figure 14 depicts the problem domain, boundary conditions, and loading protocol. All fluid phase boundaries are assumed impermeable. The porous body is discretized into 19,200 mixed points with d=0.5 mm. All material parameters are the same as adopted in Example 1. The specimen is prescribed zero initial effective stress and water pressure as assumed in Reference 13. As shown in Figure 14, the loading rate $\dot{u}_x=1\times 10^{-3}$ mm/s. The total loading time t=30 s and $\Delta t=0.02$ s. We first present the base simulation results to show the crack propagation and water pressure variation in the specimen under the shear loading. Figure 15 presents the snapshots of the contour of the damage variable φ superimposed on the deformed configuration at three loading stages. Figure 16 plots the contours of water pressure at three load stages. The results in Figure 15 indicate that the crack under the shear loading propagates upward following a slightly curved path. As shown in Figure 16, the water pressure is negative (i.e., matric suction) around the newly propagated crack and the area above the initial crack. Next, we repeat the base simulation with different horizons and m to study the influence of δ and m on the numerical results.

4.2.1 | Influence of δ

To study the influence of δ on the mode II crack propagation, we conduct the simulations using three different horizons $\delta = 1.5$, 1.2, and 0.9 mm, respectively, with m = 3. The spatial discretizations consist of 19,200, 31,000, and 53,000 mixed material points, respectively. The results are shown in Figures 17–19.

Figure 17 presents the contours of the damage variable φ for the three simulations superimposed on the deformed configuration at $u_x = 6 \times 10^{-2}$ mm. The results in Figure 17 show that the crack propagation follows a similar path for the three simulations. This is consistent with the results in Figure 19 that compare the crack path for the three cases.

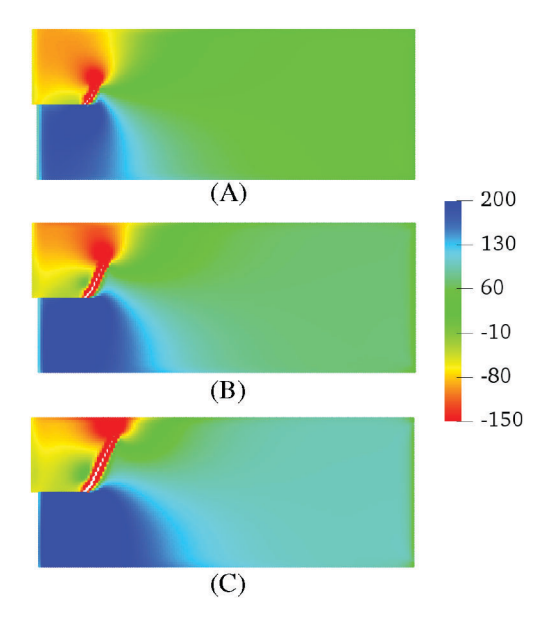


FIGURE 16 Contours of water pressure (kPa) at (A) $u_x = 2.0 \times 10^{-2}$ mm, (B) $u_x = 2.5 \times 10^{-2}$ mm, and (C) $u_x = 3.0 \times 10^{-2}$ mm (×50)

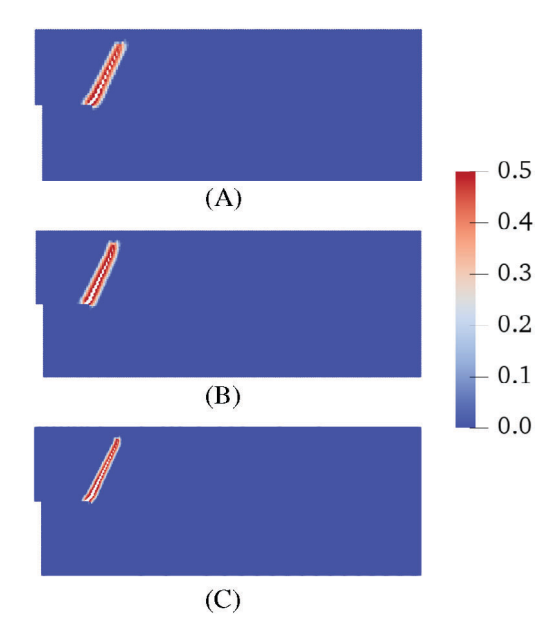


FIGURE 17 Contours of the damage variable φ from the simulations using (A) $\delta = 1.5$ mm, (B) $\delta = 1.2$ mm, and (C) $\delta = 0.9$ mm at $u_x = 3 \times 10^{-2}$ mm (×50)

Figure 18 plots the contours of water pressure in the problem domain for the three simulations. For all three cases, the water pressure around the crack and above the initial crack is negative (matric suction) and the water pressure below the initial crack is positive.

4.2.2 | Influence of m

To study the influence of m on the mode II crack propagation in porous media, we conduct simulations using m=3, 4, and 5 with $\delta=1.5$ mm. The discretizations consist of 19,200, 31,000, and 53,000 mixed material points, respectively. Figure 20 presents the contours of damage for the simulations at $u_x=3\times 10^{-2}$ mm. Figure 21 plots the contours of water pressure for the simulations. The crack paths from the three cases are compared in Figure 22.

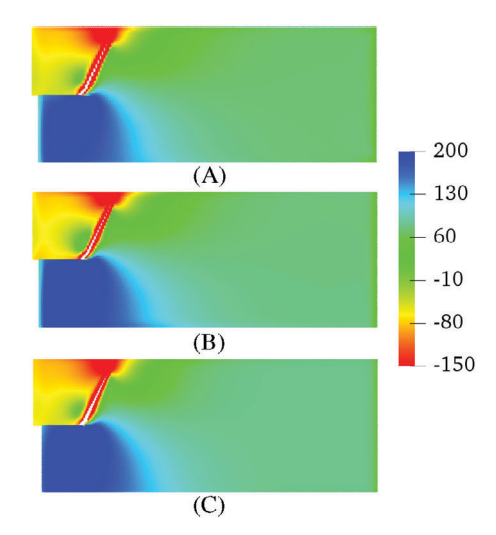


FIGURE 18 Contours of water pressure (kPa) from the simulations using (A) $\delta = 1.5$ mm, (B) $\delta = 1.2$ mm, and (C) $\delta = 0.9$ mm at $u_x = 3 \times 10^{-2}$ mm (×50)

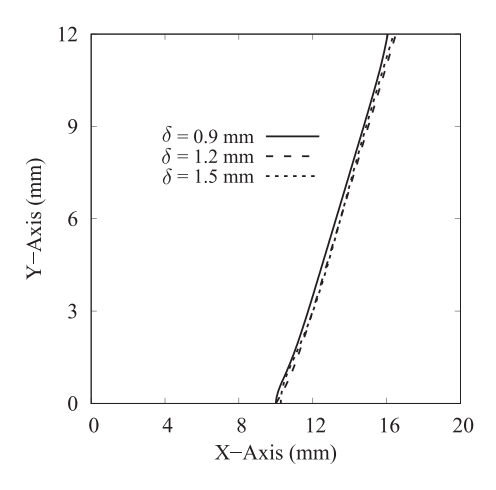


FIGURE 19 Comparison of the crack path from the simulations using different δ and m = 3

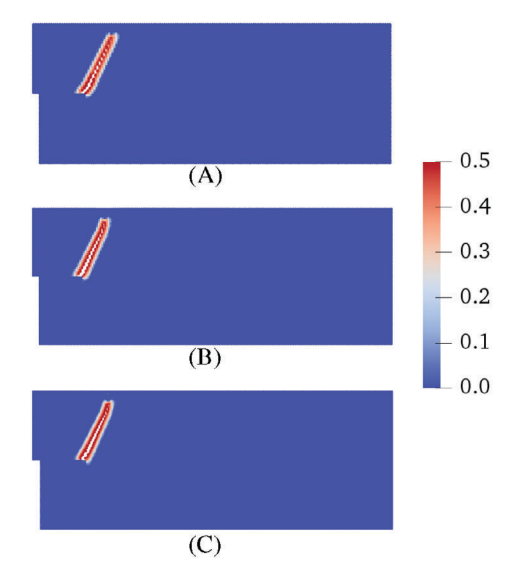


FIGURE 20 Contours of the damage variable φ from the simulations using (A) m = 3, (B) m = 4, and (C) m = 5 at $u_x = 3 \times 10^{-2}$ mm (×50)

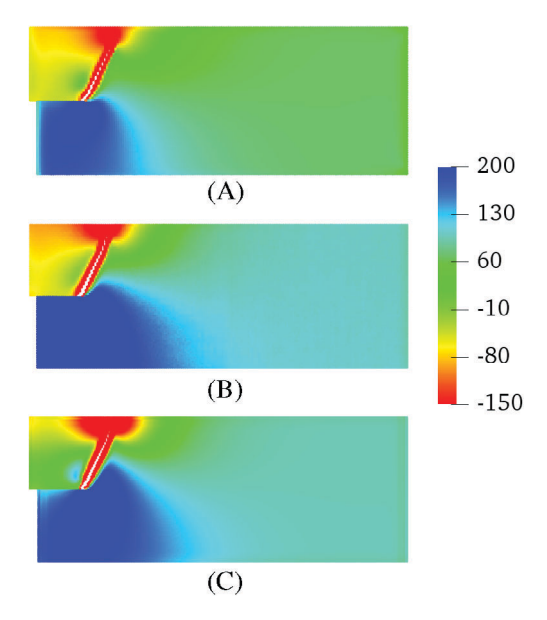


FIGURE 21 Contours of water pressure (kPa) from the simulations using (A) m = 3, (B) m = 4, and (C) m = 5 at $u_x = 3 \times 10^{-2}$ mm (×50)

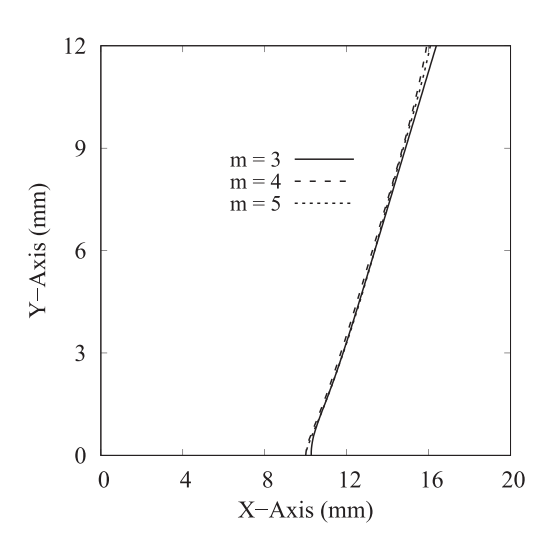


FIGURE 22 Comparison of the crack path from the simulations using (A) m = 3, (B) m = 4, and (C) m = 5 at $u_x = 3 \times 10^{-2}$ mm

It is indicated from Figure 22 that the choice of m has a mild impact on the crack propagation path. However, the value of m has a noticeable impact on the water pressure in the problem domain as shown in Figure 21. Comparison of the results in Figures 19 and 22 shows that m = 3 could be a sufficient choice for modeling unguided mode II cracks in variably saturated porous media. We note that more studies should be conducted to guide the appropriate choice of m for realistically modeling arbitrary cracks in unsaturated porous media through the proposed framework.

4.3 | Example 3: Wing crack propagation

In this example, we simulate the wing crack propagation in an unsaturated porous medium through the implemented unsaturated fracturing periporomechanics model. Figure 23 depicts the problem geometry and loading protocol. The problem domain is discretized into 20,000 uniform mixed material points with d=1 mm. The material parameters adopted are $K=70\times 10^4$ kPa, $\mu_s=15\times 10^4$ kPa, $\phi_0=0.33$, $k_w=1\times 10^{-15}$ m², n=1.5, $s_a=500$ kPa. The horizon $\delta=3.05d$. The porous body is prescribed an initial uniform effective stress -49.5 kPa and initial suction 50 kPa (i.e., the zero initial total

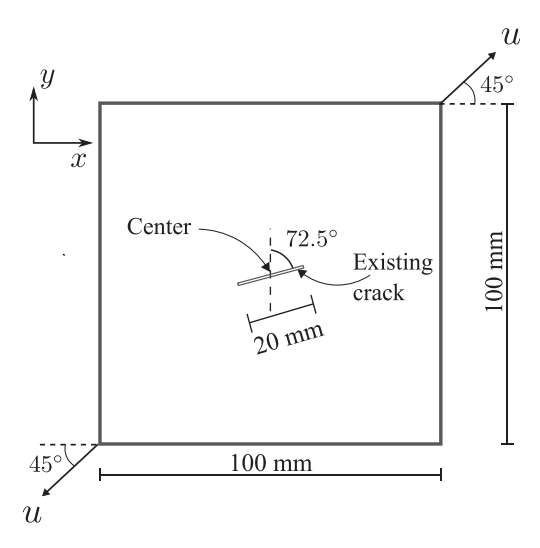


FIGURE 23 Problem setup for Example 3

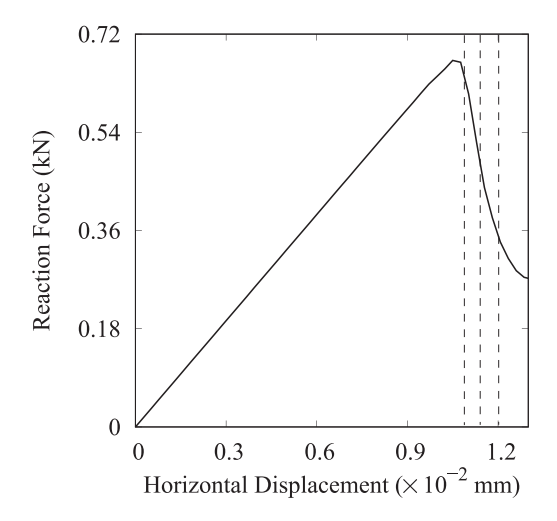


FIGURE 24 Plot of the loading curve over applied horizontal displacement

stress). $S_r = 0.99$ from (17). The loading rate $\dot{u} = 1.41 \times 10^{-5}$ mm/s as shown in Figure 23. The total loading time t = 3000 s and $\Delta t = 1$ s.

Figure 24 plots the loading curve versus the applied horizontal displacement. The vertical dash lines denote the applied displacements $u_x = u_y = (a) 1.0 \times 10^{-2}$ mm, (b) 1.1×10^{-2} mm, and (c) 1.2×10^{-2} mm. The snapshots of contours of the damage variable φ and water pressure at these three loading stages are presented in Figures 25 and 26, respectively. The results in Figure 25 show that the propagation path of the wing cracks is parallel to the diagonal line of the specimen. This crack propagation path matches the experimental result and the wing crack propagation in a single-phase solid under the same loading condition through peridynamics (e.g., References 53 and 56). The contours of water pressure in Figure 26 indicate that the crack propagation has led to the increase of matric suction around the wing cracks. This may imply that the formation rate of new fracture space is larger than the rate of the volume of water flowing into the newly formed fracture space. Therefore, the degree of saturation in the fracture space is smaller than that in the bulk (see 17). The overall low hydraulic conductivity (i.e., intrinsic permeability multiplied by the relative permeability) in the bulk under unsaturated condition could be a contributing factor for the low flow rate of water from the bulk into the fracture space. In what follows, we study the influence of initial matric suction and intrinsic permeability on the wing crack propagation by repeating the simulation with different initial matric suctions and intrinsic permeabilities while keeping other parameters unchanged.

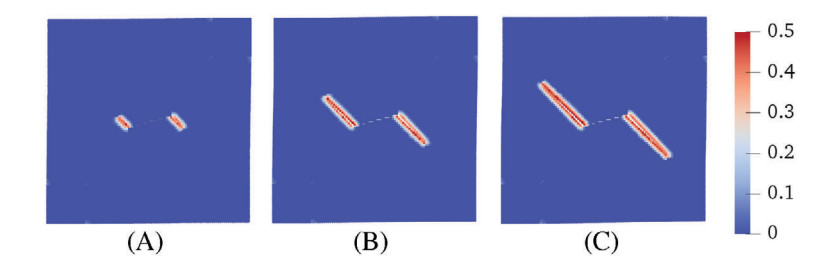


FIGURE 25 Contours of the damage variable φ superimposed on the deformed configuration at (A) $u_x = 1.0 \times 10^{-2}$ mm, (B) $u_x = 1.1 \times 10^{-2}$ mm, and (C) $u_x = 1.2 \times 10^{-2}$ mm (×50)

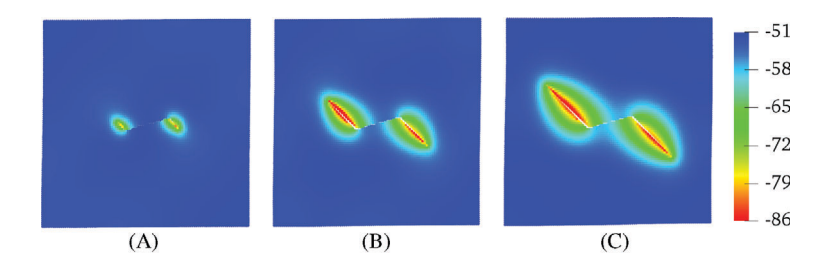


FIGURE 26 Contours of water pressure (kPa) superimposed on the deformed configuration at (A) $u_x = 1.0 \times 10^{-2}$ mm, (B) $u_x = 1.1 \times 10^{-2}$ mm, and (C) $u_x = 1.2 \times 10^{-2}$ mm (×50)

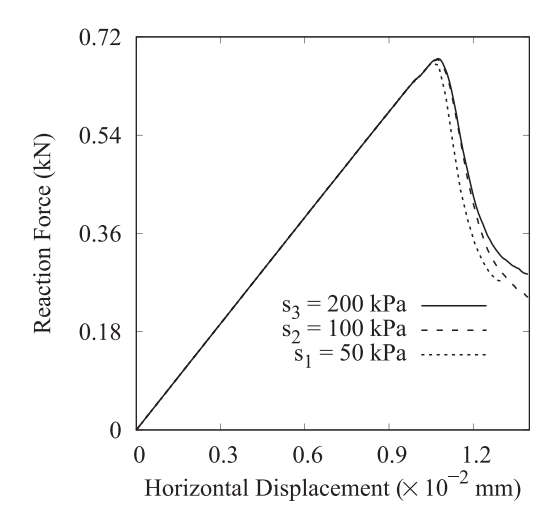


FIGURE 27 Comparison of the loading curves from the simulations with different initial matric suctions

4.3.1 | Influence of initial matric suction

To study the influence of initial matric suction on the wing crack propagation, the simulations were repeated with another two values of initial matric suction 100 and 200 kPa. To maintain the zero initial total stress condition, the corresponding initial effective stress is -96 and -180 kPa, respectively. The values of degree of saturation S_r are respectively 0.96 and 0.9. All other parameters remain unchanged.

Figure 27 plots the loading curves from the simulations with the three initial matric suctions. The initial matric suction has a mild impact on the peak loading. Once the crack propagates, the reaction load for the specimen with larger matric suction is generally larger than that with smaller initial matric suction over the loading process. This could be due to the larger tensile strength of the specimen with larger matric suction. Figures 28 and 29 present the contours of damage variable and water pressure superimposed on the deformed configuration at the same loading stage. The comparison in

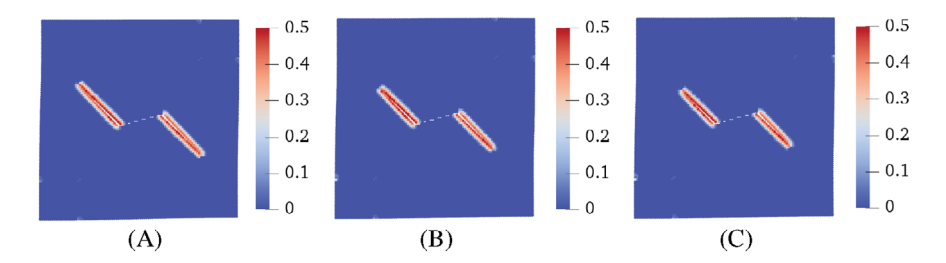


FIGURE 28 Contours of the damage variable φ from the simulations with three initial matric suctions (A) $s_1 = 50$ kPa, (B) $s_2 = 100$ kPa, and (C) $s_3 = 200$ kPa at $u_x = 1.2 \times 10^{-2}$ mm (×50)

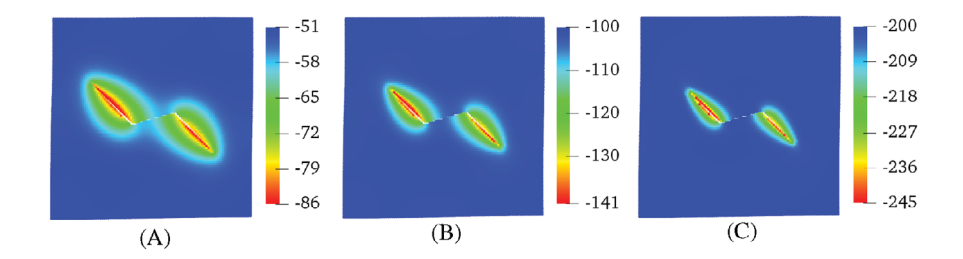


FIGURE 29 Contours of water pressure (kPa) from the simulations with three initial matric suctions (A) $s_1 = 50$ kPa, (B) $s_2 = 100$ kPa, and (C) $s_3 = 200$ kPa at $u_x = 1.2 \times 10^{-2}$ mm (×50)

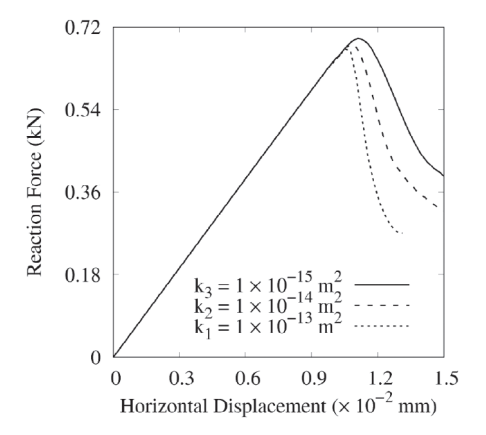


FIGURE 30 Comparison of the loading curves for the simulations with three intrinsic permeabilities

Figure 28 shows that the length of the wing cracks is correlated with the initial matric suction under the same mechanical loading stage. The wing cracks are shorter in the specimen with larger initial matric suction. The magnitude of the initial suction does not impact the direction of the wing cracks due to the isotropic assumption. As shown in Figure 29, matric suction increases around the wing cracks for the simulations with different initial matric suctions.

4.3.2 | Influence of intrinsic permeability

We study the influence of intrinsic permeability on the wing crack propagation in unsaturated porous media by comparing the results from the simulations with three intrinsic permeabilities $k_1 = 1 \times 10^{-13}$ m², $k_2 = 1 \times 10^{-14}$ m², and $k_3 = 1 \times 10^{-15}$ m². Figure 30 plots the loading curves from the three simulations. The loading curves are almost identical before the peak value from the simulation with $k_1 = 1 \times 10^{-13}$ m². After that the loading curves for the three simulations diverge from each other. For the two simulations with smaller intrinsic permeabilities the specimen has a larger peak load. For all

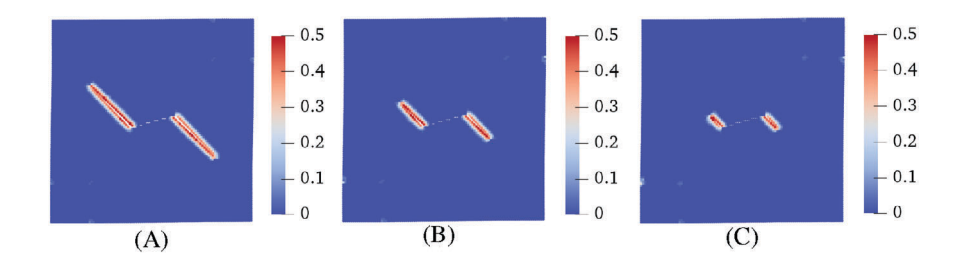


FIGURE 31 Contours of the damage variable φ for the simulations with three intrinsic permeabilities (A) $k_1 = 1 \times 10^{-13} \text{ m}^2$, (B) $k_2 = 1 \times 10^{-14} \text{ m}^2$, and (C) $k_3 = 1 \times 10^{-15} \text{ m}^2$ on the deformed configuration at $u_x = 1.2 \times 10^{-2} \text{ mm}$ (×50)

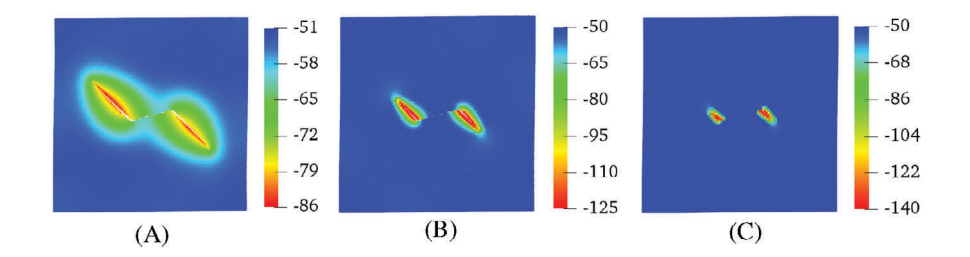


FIGURE 32 Contours of water pressure for the simulations with three intrinsic permeabilities (A) $k_1 = 1 \times 10^{-13} \text{ m}^2$, (B) $k_2 = 1 \times 10^{-14} \text{ m}^2$, and (C) $k_3 = 1 \times 10^{-15} \text{ m}^2$ on the deformed configuration at $u_x = 1.2 \times 10^{-2} \text{ mm}$ (×50)

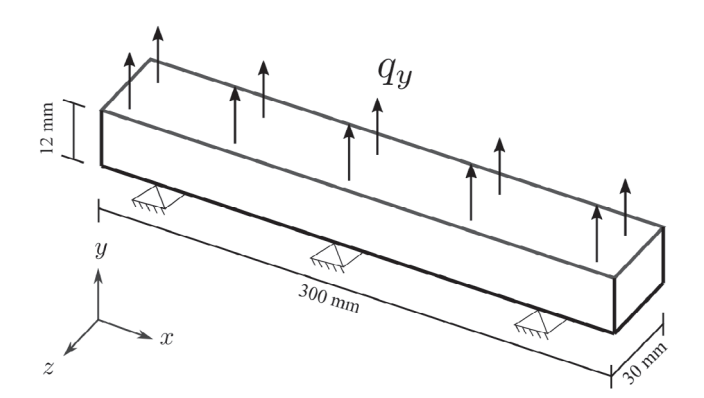


FIGURE 33 Problem setup for Example 4

three cases, the crack starts propagating at the peak load. Figures 31 and 32 plot the snapshots of the contours of damage variable and water pressure for the three simulations at the same loading stage, respectively. The results show that intrinsic permeability could have a dramatic influence on the length of wing cracks, as well as the matric suction around the wing cracks. As shown in Figure 31, at the same loading stage the length of the wing cracks from the simulation with smaller intrinsic permeability is smaller than the simulation with larger intrinsic permeability. The larger matric suction has generated around the wing crack for the simulation with smaller intrinsic permeability as shown in Figure 32. The larger matric suction may explain the reduced wing crack propagation for the simulation with smaller intrinsic permeability. The results have demonstrated that intrinsic permeability could have a significant impact on the wing crack propagation and the matric suction around the wing crack in unsaturated porous media.

4.4 | Example 4: Nonplanar cracking in an unsaturated parallelepiped soil specimen

In this example, we simulate the formation of nonplanar cracks in an unsaturated parallelepiped soil specimen triggered by matric suction variations. Figure 33 sketches the problem setup and boundary conditions. The problem domain is

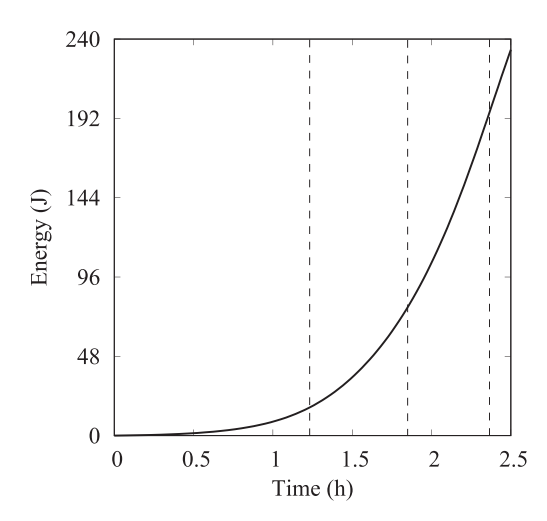


FIGURE 34 Plot of the total energy dissipation over time due to the crack formation

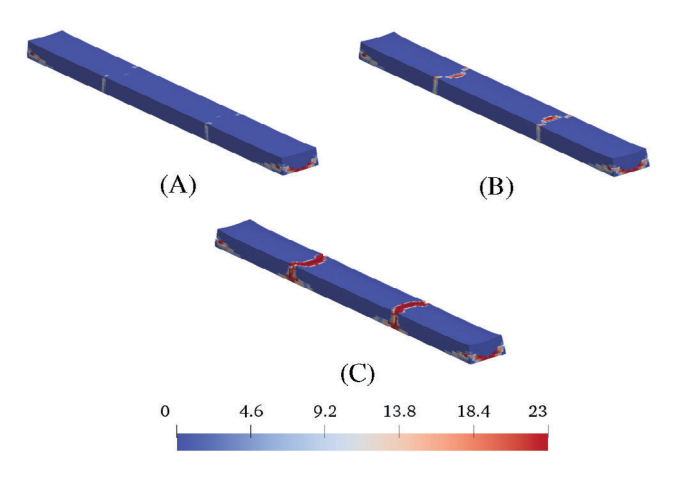


FIGURE 35 Contours of the energy dissipation density due to bond breakage (MJ/m³) superimposed on the deformed configuration at (A) t = 1.2 h, (B) t = 1.8 h, and (C) t = 2.3 h

discretized into 20,000 mixed points with d=1.8 mm. The material parameters adopted are $K=5\times 10^3$ kPa, $\mu_s=2.1\times 10^3$ kPa, $\phi_0=0.1$, $G_c=0.5$ J/m², $k_w=1\times 10^{-14}$ m², n=1.25, $s_a=100$ kPa. The horizon $\delta=3.05$ d. The initial uniform effective stress in the specimen is assumed -47 kPa. The initial matric suction is assumed 50 kPa and $S_r=0.94$ from (17). In this case, the initial total stress in the specimen is null. A water flow boundary with a constant density rate $q_y=1.5$ kg/(m³ s) is imposed on the top surface through a fictitious boundary layer with the thickness of δ . Specifically, this constant flow density rate is assigned on all the material points in the fictitious boundary layer. The total flow rate on the top boundary is equal to the flow density rate q_y multiplied by the volume of the boundary layer. All other fluid boundaries are impermeable. The total simulation time t=3 h and $\Delta t=1$ s.

First, we present the energy dissipation characteristics due to the formation of nonplanar cracks in the specimen. We note that the dissipated energy due to bond breakage is determined from (37) based on the effective force state concept. The dissipated energy density represents the energy consumed due to bond breakage at a material point. Figure 34 shows the total energy dissipation over the simulation time due to bond breakage. Here the total energy dissipation in the specimen is defined as the summation of the energy dissipation at all fracture points. Figure 35 presents the snapshots of the contour of dissipated energy associated with the bond breakage and the formation of nonplanar cracks at three load steps denoted in Figure 34. The results demonstrate that the energy dissipation rate due to bond breakage has increased dramatically upon the inception and propagation of cracks.

Second, we present the zoom-in snapshots of nonplanar crack topology and the contour of matric suction in the specimen. The results are shown in Figures 36–38. Figure 36 plots the contours of the horizontal displacement and the

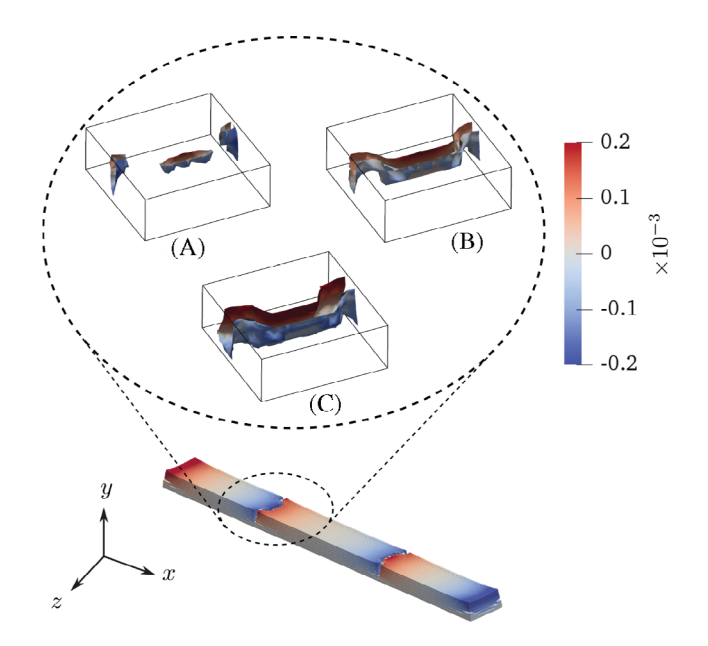


FIGURE 36 Snapshots of the contour of the horizontal displacement u_x (m) and zoom-in crack topology at (A) t = 1.2 h, (B) t = 1.8 h, and (C) t = 2.3 h

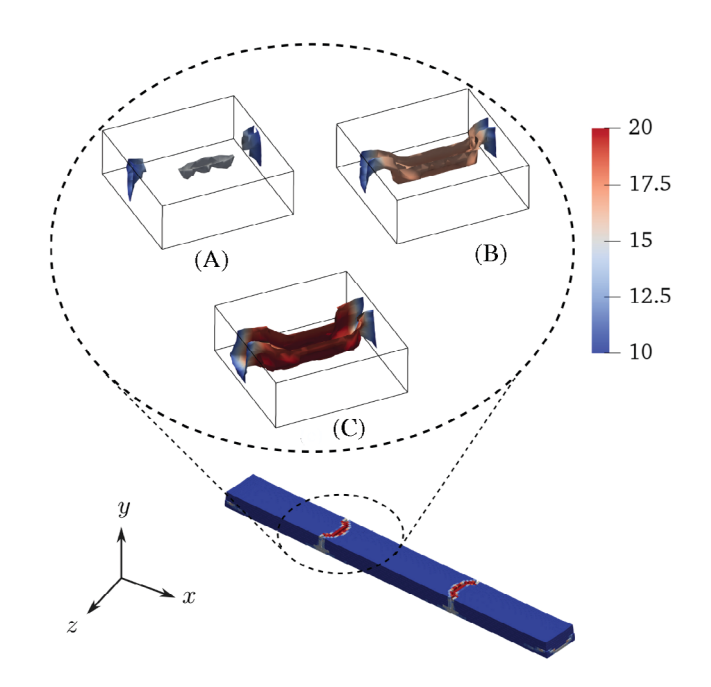


FIGURE 37 Snapshots of the contour of dissipation energy density (MJ/m³) superimposed on the zoom-in crack topology at (A) t = 1.2 h, (B) t = 1.8 h, and (C) t = 2.3 h

zoom-in crack topology at three time steps. Figure 37 depicts the snapshots of the dissipation energy density on the crack surface in the deformed configuration. Two major nonplanar cracks have formed in the specimen due to the shrinkage in the *x* direction. Figure 36 demonstrates that the two major cracks initiate on the top and side surfaces and then propagate downward within the specimen. Figure 38 plots the contours of water pressure (or negative matric suction) on the crack surface. The matric suction on the top surface is the largest due to the outward water flow boundary condition. From the results in Figures 36 and 38, we could conclude that in this example the nonplanar cracks within the specimen have been triggered by the increasing matric suction from the top surface. We note that the retention mechanism of water could play an important role in crack growth^{75,76} that deserves further study, which is beyond the scope of this article. In summary,

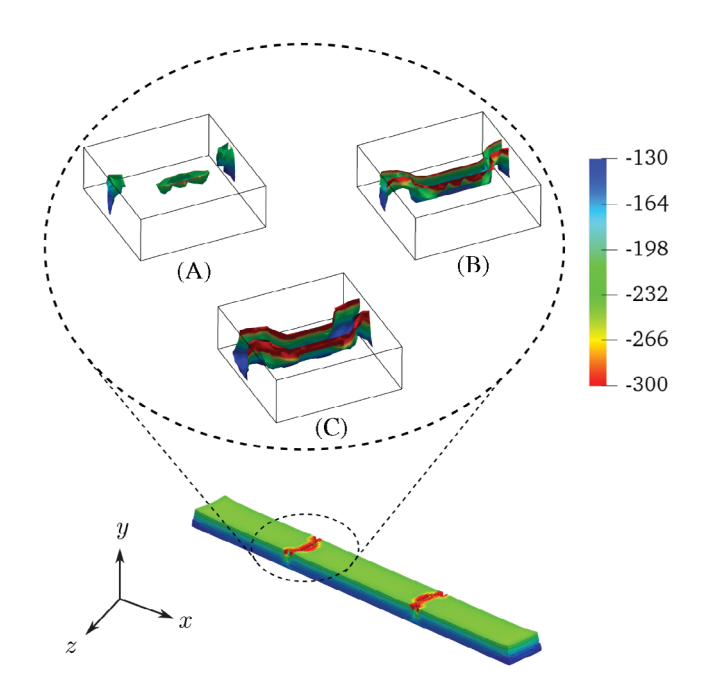


FIGURE 38 Snapshots of the contour of water pressure (kPa) superimposed on the zoom-in crack topology in the deformed configuration at (A) t = 1.2 h, (B) t = 1.8 h, and (C) t = 2.3 h

through this example we have demonstrated the efficacy of the proposed fracturing periporomechanics framework for modeling unguided nonplanar cracking in unsaturated porous media.

5 | CLOSURE

In this article, as a new contribution we have formulated and implemented an unsaturated fracturing periporomechanics framework for unguided cracking in unsaturated porous media. In this new coupled periporomechanics paradigm crack nucleation and propagation are modeled by an effective force based criterion that incorporates the effect of matric suction on cracking. It is noted that crack formation is completely autonomous and requires no external criteria nor a priori knowledge/assumption of the crack path. Unsaturated fluid flow in the fracture space is modeled via a simplified formation in line with the unsaturated fluid flow in the bulk. A fractional step algorithm via the celebrated two-stage operator split and a two-phase mixed meshless method are utilized to solve the coupled fracturing periporomechanics paradigm. At each time step, an undrained deformation stage of the skeleton by fixing fluid flow is solved first, and then unsaturated fluid mass transport is solved in the updated fractured skeleton configuration. The implementation of the coupled fracturing periporomechanics paradigm has been validated using numerical examples based on the extended finite element method in the literature. Through the numerical simulations, we have demonstrated the capability and robustness of the proposed nonlocal poromechanics in modeling mode I and mode II crack propagation in unsaturated porous media. The efficacy of the fracturing unsaturated periporomechanics paradigm for nonplanar cracks has been demonstrated by modeling unguided cracking in a three-dimensional soil specimen triggered by matric suction variations.

ACKNOWLEDGMENTS

This work has been supported by the US National Science Foundation under contract numbers 1659932 and 1944009. The support is greatly acknowledged. The authors are grateful to the two anonymous reviewers for their expert reviews of the original version of this article.

ORCID

Xiaoyu Song https://orcid.org/0000-0003-0409-3761

REFERENCES

- 1. Terzaghi K, Peck RB, Mesri G. Soil Mechanics in Engineering Practice. John Wiley & Sons; 1996.
- 2. Fredlund DG, Rahardjo H. Soil Mechanics for Unsaturated Soils. John Wiley & Sons; 1993.
- 3. Lu N, Likos WJ. Unsaturated Soil Mechanics. John Wiley & Sons; 2004.
- 4. Borja RI, Song X, Wu W. Critical state plasticity. Part VII: triggering a shear band in variably saturated porous media. *Comput Methods Appl Mech Eng.* 2013;261:66-82.
- 5. Song X, Ye M, Wang K. Strain localization in a solid-water-air system with random heterogeneity via stabilized mixed finite elements. *Int J Numer Methods Eng.* 2017;112(13):1926-1950.
- 6. Song X, Wang K, Ye M. Localized failure in unsaturated soils under non-isothermal conditions. Acta Geotech. 2018;13(1):73-85.
- 7. Song X, Wang K, Bate B. A hierarchical thermo-hydro-plastic constitutive model for unsaturated soils and its numerical implementation. *Int J Numer Anal Methods Geomech.* 2018;42(15):1785-1805.
- 8. Song X, Wang MC. Molecular dynamics modeling of a partially saturated clay-water system at finite temperature. *Int J Numer Anal Methods Geomech.* 2019;43(13):2129-2146.
- 9. Likos WJ, Song X, Xiao M, Cerato A, Lu N. Fundamental challenges in unsaturated soil mechanics. In: Lu N, Mitchell J, eds. *Geotechnical Fundamentals for Addressing New World Challenges*. Springer; 2019:209-236.
- 10. Wang K, Song X. Strain localization in non-isothermal unsaturated porous media considering material heterogeneity with stabilized mixed finite elements. *Comput Methods Appl Mech Eng.* 2020;359:112770.
- 11. Song X, Zhang Z. Determination of clay-water contact angle via molecular dynamics and deep-learning enhanced methods. *Acta Geotech*. 2021:1-15.
- 12. Alonso EE. Triggering and motion of landslides. Géotechnique. 2021;71(1):3-59.
- 13. de Borst R. Computational Methods for Fracture in Porous Media: Isogeometric and Extended Finite Element Methods. Elsevier; 2017.
- 14. Khoei AR. Extended Finite Element Method: Theory and Applications. John Wiley & Sons; 2014.
- 15. Menon S, Song X. Coupled analysis of desiccation cracking in unsaturated soils through a non-local mathematical formulation. *Geosciences*. 2019;9(10):428.
- 16. Albrecht BA, Benson CH. Effect of desiccation on compacted natural clays. J Geotech Geoenviron Eng. 2001;127(1):67-75.
- 17. Moës N, Dolbow J, Belytschko T. A finite element method for crack growth without remeshing. *Int J Numer Methods Eng.* 1999;46(1):131-150.
- 18. Sukumar N, Moës N, Moran B, Belytschko T. Extended finite element method for three-dimensional crack modelling. *Int J Numer Methods Eng.* 2000;48(11):1549-1570.
- 19. Menon S, Song X. Shear banding in unsaturated geomaterials through a strong nonlocal hydromechanical model. *Eur J Environ Civil Eng.* 2020;1-15.
- 20. Song X, Khalili N. A peridynamics model for strain localization analysis of geomaterials. *Int J Numer Anal Methods Geomech*. 2019;43(1):77-96.
- 21. Song X, Menon S. Modeling of chemo-hydromechanical behavior of unsaturated porous media: a nonlocal approach based on integral equations. *Acta Geotech.* 2019;14(3):727-747.
- 22. Song X, Silling S. On the peridynamic effective force state and multiphase constitutive correspondence principle. *J Mech Phys Solids*. 2020;104161.
- 23. Menon S, Song X. A computational periporomechanics model for localized failure in unsaturated porous media. *Comput Methods Appl Mech Eng.* 2021;384:113932.
- 24. Menon S, Song X. A stabilized computational nonlocal poromechanics model for dynamic analysis of saturated porous media. *Int J Numer Methods Eng.* 2021.
- 25. Lewis RW, Schrefler B. The Finite Element Method in the Static and Dynamic Deformation and Consolidation of Porous Media. John Wiley & Sons; 1998.
- 26. Zienkiewicz OC, Chan A, Pastor M, Schrefler B, Shiomi T. Computational Geomechanics. Vol 613. Citeseer; 1999.
- 27. Coussy O. Poromechanics. John Wiley & Sons; 2004.
- 28. Silling SA. Reformulation of elasticity theory for discontinuities and long-range forces. J Mech Phys Solids. 2000;48(1):175-209.
- 29. Silling SA, Epton M, Weckner O, Xu J, Askari E. Peridynamic states and constitutive modeling. J Elasticity. 2007;88(2):151-184.
- 30. Silling S. Dynamic fracture modeling with a meshfree peridynamic code. In: Bathe KJ, ed. *Computational Fluid and Solid Mechanics*. Elsevier; 2003:641-644.
- 31. Silling SA, Weckner O, Askari E, Bobaru F. Crack nucleation in a peridynamic solid. Int J Fract. 2010;162(1-2):219-227.
- 32. Agwai A, Guven I, Madenci E. Predicting crack propagation with peridynamics: a comparative study. Int J Fract. 2011;171(1):65.
- 33. Anderson TL, Anderson T. Fracture Mechanics: Fundamentals and Applications. CRC Press; 2005.
- 34. Silling SA, Askari E. A meshfree method based on the peridynamic model of solid mechanics. Comput Struct. 2005;83(17-18):1526-1535.
- 35. Warren TL, Silling SA, Askari A, Weckner O, Epton MA, Xu J. A non-ordinary state-based peridynamic method to model solid material deformation and fracture. *Int J Solids Struct*. 2009;46(5):1186-1195.
- 36. Xu J, Askari A, Weckner O, Silling S. Peridynamic analysis of impact damage in composite laminates. J Aerosp Eng. 2008;21(3):187-194.
- 37. Kilic B, Agwai A, Madenci E. Peridynamic theory for progressive damage prediction in center-cracked composite laminates. *Compos Struct*. 2009;90(2):141-151.
- 38. Gerstle W, Sau N, Silling S. Peridynamic modeling of concrete structures. Nucl Eng Des. 2007;237(12-13):1250-1258.

- 39. Bobaru F, Duangpanya M. A peridynamic formulation for transient heat conduction in bodies with evolving discontinuities. *J Comput Phys.* 2012;231(7):2764-2785.
- 40. Zhang H, Qiao P. An extended state-based peridynamic model for damage growth prediction of bimaterial structures under thermomechanical loading. *Eng Fract Mech.* 2018;189:81-97.
- 41. Ouchi H, Katiyar A, York J, Foster JT, Sharma MM. A fully coupled porous flow and geomechanics model for fluid driven cracks: a peridynamics approach. *Comput Mech.* 2015;55(3):561-576.
- 42. Oterkus S, Madenci E, Oterkus E. Fully coupled poroelastic peridynamic formulation for fluid-filled fractures. Eng Geol. 2017;225:19-28.
- 43. Zhang H, Qiao P. A coupled peridynamic strength and fracture criterion for open-hole failure analysis of plates under tensile load. *Eng Fract Mech.* 2018;204:103-118.
- 44. Ni T, Pesavento F, Zaccariotto M, Galvanetto U, Zhu QZ, Schrefler BA. Hybrid fem and peridynamic simulation of hydraulic fracture propagation in saturated porous media. *Comput Methods Appl Mech Eng.* 2020;366:113101.
- 45. Sun W, Fish J. Coupling of non-ordinary state-based peridynamics and finite element method for fracture propagation in saturated porous media. *Int J Numer Anal Methods Geomech.* 2021.
- 46. Kilic B, Madenci E. Prediction of crack paths in a quenched glass plate by using peridynamic theory. Int J Fract. 2009;156(2):165-177.
- 47. Bobaru F, Zhang G. Why do cracks branch? A peridynamic investigation of dynamic brittle fracture. *Int J Fract.* 2015;196(1-2):59-98.
- 48. Hu W, Ha YD, Bobaru F. Peridynamic model for dynamic fracture in unidirectional fiber-reinforced composites. *Comput Methods Appl Mech Eng.* 2012;217:247-261.
- 49. Li P, Hao Z, Yu S, Zhen W. Implicit implementation of the stabilized non-ordinary state-based peridynamic model. *Int J Numer Methods Eng.* 2020;121(4):571-587.
- 50. Foster JT, Silling SA, Chen W. An energy based failure criterion for use with peridynamic states. *Int J Multiscale Comput Eng.* 2011;9(6):675-688.
- 51. Breitenfeld M, Geubelle P, Weckner O, Silling S. Non-ordinary state-based peridynamic analysis of stationary crack problems. *Comput Methods Appl Mech Eng.* 2014;272:233-250.
- 52. Madenci E, Oterkus S. Ordinary state-based peridynamics for plastic deformation according to von mises yield criteria with isotropic hardening. *J Mech Phys Solids*. 2016;86:192-219.
- 53. Lipton RP, Lehoucq RB, Jha PK. Complex fracture nucleation and evolution with nonlocal elastodynamics. *J Peridyn Nonlocal Model*. 2019;1(2):122-130.
- 54. Rice JR. A path independent integral and the approximate analysis of strain concentration by notches and cracks. *J Appl Mech.* 1968;35(2):379-386.
- 55. Ni T, Pesavento F, Zaccariotto M, Galvanetto U, Schrefler BA. Numerical simulation of forerunning fracture in saturated porous solids with hybrid fem/peridynamic model. *Comput Geotech.* 2021;133:104024.
- 56. Madenci E, Oterkus E. Peridynamic Theory and Its Applications. Springer; 2014.
- 57. Simoni L, Schrefler B. A staggered finite-element solution for water and gas flow in deforming porous media. *Commun Appl Numer Methods*. 1991;7(3):213-223.
- 58. Simo J, Miehe C. Associative coupled thermoplasticity at finite strains: formulation, numerical analysis and implementation. *Comput Methods Appl Mech Eng.* 1992;98(1):41-104.
- 59. Armero F, Simo J. A new unconditionally stable fractional step method for non-linear coupled thermomechanical problems. *Int J Numer Methods Eng.* 1992;35(4):737-766.
- 60. Kilic B, Madenci E. Structural stability and failure analysis using peridynamic theory. Int J Non-Linear Mech. 2009;44(8):845-854.
- 61. Kilic B, Madenci E. An adaptive dynamic relaxation method for quasi-static simulations using the peridynamic theory. *Theor Appl Fract Mech.* 2010;53(3):194-204.
- 62. Ni T, Zaccariotto M, Zhu QZ, Galvanetto U. Static solution of crack propagation problems in peridynamics. *Comput Methods Appl Mech Eng.* 2019;346:126-151.
- 63. Gu X, Zhang Q, Madenci E. Non-ordinary state-based peridynamic simulation of elastoplastic deformation and dynamic cracking of polycrystal. *Eng Fract Mech.* 2019;218:106568.
- 64. Song X, Borja RI. Mathematical framework for unsaturated flow in the finite deformation range. *Int J Numer Methods Eng.* 2014;97(9):658-682.
- 65. Song X. Transient bifurcation condition of partially saturated porous media at finite strain. *Int J Numer Anal Methods Geomech.* 2017;41(1):135-156.
- 66. Song X, Borja RI. Finite deformation and fluid flow in unsaturated soils with random heterogeneity. Vadose Zone J. 2014;13(5):1-11.
- 67. Cao J, Jung J, Song X, Bate B. On the soil water characteristic curves of poorly graded granular materials in aqueous polymer solutions. *Acta Geotech.* 2018;13(1):103-116.
- 68. Niu WJ, Ye WM, Song X. Unsaturated permeability of gaomiaozi bentonite under partially free-swelling conditions. *Acta Geotech*. 2020;15(5):1095-1124.
- Van Genuchten MT. A closed-form equation for predicting the hydraulic conductivity of unsaturated soils. Soil Sci Soc Am J. 1980;44(5):892-898.
- 70. Silling SA. Stability of peridynamic correspondence material models and their particle discretizations. *Comput Methods Appl Mech Eng.* 2017;322:42-57.
- 71. Katiyar A, Foster JT, Ouchi H, Sharma MM. A peridynamic formulation of pressure driven convective fluid transport in porous media. *J Comput Phys.* 2014;261:209-229.

- 72. Turska E, Schrefler B. On convergence conditions of partitioned solution procedures for consolidation problems. *Comput Methods Appl Meth Eng.* 1993;106(1-2):51-63.
- 73. Hughes TJ. The Finite Element Method: Linear Static and Dynamic Finite Element Analysis. Courier Corporation; 2012.
- 74. Réthoré J, De Borst R, Abellan MA. A two-scale model for fluid flow in an unsaturated porous medium with cohesive cracks. *Comput Mech.* 2008;42(2):227-238.
- 75. Cajuhi T, Sanavia L, De Lorenzis L. Phase-field modeling of fracture in variably saturated porous media. Comput Mech. 2018;61(3):299-318.
- 76. Heider Y, Sun W. A phase field framework for capillary-induced fracture in unsaturated porous media: drying-induced vs. Hydraulic cracking. *Comput Methods Appl Mech Eng.* 2020;359:112647.

How to cite this article: Menon S, Song X. Computational multiphase periporomechanics for unguided cracking in unsaturated porous media. *Int J Numer Methods Eng.* 2022;123(12):2837-2871. doi: 10.1002/nme.6961